THE APPROACH OF IMPROVING THE ROLL CONTROL OF A SLOCUM AUTONOMOUS UNDERWATER GLIDER

MINGXI ZHOU

The Approach of Improving the Roll Control of a Slocum Autonomous Underwater Glider

by

©Mingxi Zhou

A Thesis submitted to the School of Graduate Studies in partial fulfillment of the requirements for the degree of

Master of Engineering

Faculty of Engineering and Applied Science

Memorial University of Newfoundland

September, 2012

St. John's Newfoundland

Abstract

Currently, Slocum Autonomous Underwater Gliders (AUGs) are widely used in oceanogeographic research. However, compared to the other legacy AUGs, Spray gliders and Seagliders, the roll controllability is insufficient on the Slocum gliders. This thesis discusses two different approaches of improving the roll controllability on a Slocum underwater glider. With improved roll motion, the Slocum glider has the potential to be involved in iceberg management along the Newfoundland and Labrador coast, and to fulfill the mission of iceberg surveillance and data reporting; for example, iceberg draft measurement and profiling. The operation of a Slocum glider will be safer and less expensive than the current ship based method. A simplified dynamic model of an underwater glider is derived and evaluated by comparing the simulation result with the field trial data collected in Conception Bay, Newfoundland and Labrador, Canada, 2010. The presented dynamic model can be easily modified to represent various realistic Slocum glider internal mass arrangements or even other types of Autonomous Underwater Vehicles (AUVs). In addition to the existing internal structure of a Slocum glider, a movable mass, the position of which is variable in the wingspan direction, is introduced to investigate the 6 degree of freedom (DOF) performance of a Slocum glider, especially the roll and yaw motions. Two roll control mechanisms are introduced in this thesis. Based on the field data, a small roll angle (2^o to 5^o) exists in the mission due to a small error of separation between the center of buoyancy and the center of gravity in the roll trimming or other environmental effects. An Autonomous Roll Trimming Mechanism (ARTM) evolving from the wingspan movable mass is designed to simplify the roll trimming process and to eliminate the dynamic roll angle error during the flight. In the design of the Deflectable Wingtip Mechanism(DWM), the standard flat-plate wing sets are replaced by NACA0012 airfoil sections and deflectable wingtips. A miniature geared stepper motor is integrated into the wing to control the wingtip deflection angle. The mechanism rolls the glider by reversing the lift forces on the wingtips which create a rolling moment and roll the Slocum glider with an angle up to 45^o. Simulated with the previously introduced and evaluated dynamic model, the Slocum glider flies in a spiral motion with a fixed roll angle with a deflection on the wingtip. In order to control the spiral motion properly, the spiral parameters, such as turning radius and roll angle, are further examined. We illustrated the relationship between the angle of attack of the wingtip and the spiral motion performance.

Beyond the mathematical analysis of the DWM, a hydrodynamic test is applied on the DWM. A hydrodynamic testing platform is designed, on which the angle of attack of the DWM, the sweep angle, and the wingtip deflection angle are variable. The experiments are conducted in the open water flume tank located at the Engineering Department of Memorial University of Newfoundland. The forces and torques are collected using a 3-axis JR3 load cell. As a result, the hydrodynamic characteristics of the DWM with different experimental setups are obtained and compared.

Acknowledgements

This thesis includes all the research I have done in the Autonomous Ocean System Laboratory (AOSL) for my master's degree. First of all, I want to express my sincere gratitude to my supervisor, Professor Ralf Bachmayer, who provided me the opportunity of doing research in underwater technology, which I really enjoyed. Professor Ralf Bachmayer's insightful advice and sense of humour have had a great influence on my research and life.

Also, I want to thank my research colleagues in the AOSL: Brian Claus who helped me with the composite matrial in the wing fabrication and provided the Slocum glider field trial data; Haibin Wang who gave me some good advice on the mechanical designing; Zhi Li who taught me some useful tips in my electrical designing and programming; as well as Reza Chini who provided me advice in flow simulation and foil hydrodynamics. Also I want to thank David Snook and Memorial University's Technical Services for manufacturing my mechanical parts.

Finally, I want to thank my spportive family: my dear parents, Uncle Ou, Aunt Zhou, my cousin Linda, and my friends: Yehan Wang, Juwei Ge, Ling Peng and etc.. I had an enjoyable time in the last two years.

Table of Contents

List of Tables

List of Figures

List of Abbreviations

AOA	Angle of Attack
AOSL	Autonomous Ocean System Laboratory
ARTM	Autonomous Roll Trimming Mechanism
AUG	Autonomous Underwater Glider
AUV	Autonomous Underwater Vehicle
CB	Center of Buoyancy
CBS	Conception Bay South
CFD	Computational Fluid Dynamics
CG	Center of Gravity
CNLOPB	Canada Newfoundland and Labrador Offshore Petroleum Board
DOF	Degree of Freedom
DWM	Deflectable Wingtip Mechanism
MUN	Memorial University of Newfoundland
NACA	National Advisory Committee for Aeronautics
NL	Newfoundland and Labrador
NRC-IOT	National Research Council Institute for Ocean Technology
PID	Proportional Integral Derivative
SPI	Serial Peripheral Interface
UART	Universal Asynchronous Receiver/Transmitter
UAV	Unmanned Aerial Vehicle
VSMW	Variable Span Morphing Wing

List of Symbols

Symbol	Definition
α	Angle of attack
β	Sideslip angle
$\mathbf{b}$	The displacement of the glider in the Earth Fixed Coordinate
$\mathbf{b}_i$	The displacement of mass m_i in the Earth Fixed Coordinate
b1, b2, b3	3 axes of the Body Fixed Coordinate
$\boldsymbol{C}_{3\times3}$ and $\boldsymbol{D}_{3\times3}$	Cross term matrix in Dynamic Equation
C_{DW} and C_D	Drag coefficient of NACA0012 obtained in JAVAfoil and Experiment
C_{LW} and C_L	Lift coefficient of NACA0012 obtained in JAVAfoil and Experiment
D, L and SF	Drag force, Lift force and Sideslip force of the glider
D_W and L_W	The drag force and lift force on the wingtip
D_e	The disturbance in the roll direction
e1, e2, e3	3 axes of the Earth Fixed Coordinate
$\mathbf{F}_{ext}$ and $\mathbf{T}_{ext}$	Hydrodynamic forces and Torques in the Wind/Flow Coordinate
$\boldsymbol{f}_{ext}$ and $\boldsymbol{t}_{ext}$	Hydrodynamic forces and Torques in the Earth Fixed Coordinate
$\boldsymbol{f}_{gi}$	gravitational force of mass m_i

$\mathbf{J}_s$	moment of inertia matrix of stationary mass
$\boldsymbol{M}_{3\times3}$ and $\boldsymbol{J}_{3\times3}$	Overall Mass inertia and moment of inertia matrix
$\mathbf{M}_{added}$ and $\mathbf{J}_{added}$	Hydrodynamic added Mass and inertia matrix
$M_{DL1}, M_{DL2}, M_{DL3}$	Hydrodynamic roll, pitch, and yaw moment
M_{wing}	The roll torque induced by the wingtip
m	General case mass
m_b	Ballast tank mass
m_{bb}	After battery mass
m_d	The mass of the water displacement
m_h	Hull mass
$m_{movable}$	Movable mass
m_o	Net buoyancy, $m_o = m_{total} - m_d$
m_{offset}	Offset mass
m_{pb}	Pitch battery pack
m_s	Stationary mass
m_t	Trim mass
m_{total}	Total mass
μ_{SW}	The dynamic viscosity of salt water
N	Normal force on the wingtip
$\boldsymbol{\Omega}$	Angular velocity in the Earth Fixed Coordinate, $(\omega_1, \omega_2, \omega_3)^T$
$\boldsymbol{\omega}$	Angular velocity in the Body Fixed Coordinate, $(p, q, r)^T$
$\boldsymbol{P}$ and $\boldsymbol{L}$	Linear and angular inertia in the Body Fixed Coordinate
$\boldsymbol{p}$ and $\boldsymbol{l}$	Linear and angular inertia in the Earth Fixed Coordinate
$\boldsymbol{P}_m$ and $\boldsymbol{L}_m$	The linear and angular momentum cross term of a mass m
P	Parallel force on the wingtip
p_t	Inertia of the trim weight

$\mathbf{R}_{BE}$	Rotation matrix from the Body Fixed Coordinate to the Earth Fixed Coordinate
$\mathbf{R}_{BW}$	Rotation matrix from the Body Fixed Coordinate to the Wind/Flow Coordinate
$\mathbf{R}_{EB}$	Rotation matrix from the Earth Fixed Coordinate to the Body Fixed Coordinate
$\mathbf{R}_{WE}$	Rotation matrix from the Wind/Flow Coordinate to the Earth Fixed Coordinate
Re	Reynolds Number
$\mathbf{r}$	The radius of the rotation of a mass m
r_{bb}	The location after battery pack in b2 direction
$\mathbf{r}_i$	The displacement of mass m_i in the Earth Fixed Coordinate
r_Z	The b3 location of the gravity force of the total mass exclude the trim mass
$\mathbf{r}_{movable}$	The displacement of movable mass in the Body Fixed Coordinate
$\mathbf{r}_{offset}$	The displacement of offset mass in the Body Fixed Coordinate
r_{tipy}	Center of wingtip in b2 direction
r_{ty}	Trim weight offset in the b2 direction
ϕ ,θ and ψ	Roll , Pitch and Yaw angle
ρ_{SW}	Salt water density
s_{offset}	The force arm of the mis-trim mass
$\boldsymbol{v}$	Translational velocity in the Body Fixed Coordinate, $\boldsymbol{v} = (u, v, w)^T$
V	Translational velocity of the glider in the Body Fixed Coordinate
w1, w2, w3	3 axes of the Earth Fixed Coordinate
$\hat{\boldsymbol{x}}$	Defined that $\hat{\boldsymbol{x}} \cdot \boldsymbol{y} = \boldsymbol{x} \times \boldsymbol{y}$

Chapter 1

Introduction

1.1 Autonomous Underwater Vehicles (AUVs) and Autonomous Underwater Gliders (AUGs)

An Autonomous Underwater Vehicle (AUV) is a robotic device that is piloted by an onboard computer without direct human intervention. Environmental information is collected by the sensors on the AUV during a mission. As interest in ocean environments increases, the AUV is becoming one of the primary pieces of equipment employed in oceanographic studies. M. Moline et. al. [1] used an AUV for monitoring the water environment in San Diego Bay. In 2007, UBC-Gavia, a small untethered and preprogrammed AUV was assigned a series of missions for investigating the thermal structure under the ice [2]. Also the R2D4 [3], invented by the University of Tokyo Institute of Industrial Science was deployed to observe an undersea volcano. The Seaglider was employed in 2011 for a more challenging mission. It operated under the ice in the Ross Sea, Antarctica to observe a phytoplankton bloom[6].
Among the AUV categories, propeller driven and buoyancy driven AUVs, the buoyancy driven Autonomous Underwater Glider (AUG) is one of the most popular and

Table 1.1: Specification of Three Commercially Available Autonomous Underwater Gliders

	Slocum Glider	Seaglider	Spray
Manufacture	Teledyne Webb Research	iRobot Maritime System	Bluefin Robotics
Dimension[m] (L.W.H)	1.8x1x0.5	1.8x1x0.3	2.1x1x0.3
Weight[kg]	52 or 60	52	52
Max Depth[m]	1,200	1,000	1,500
Duration[hour]	720	7200	4320
Speed[m/s]	0.4	0.25	0.2
Controllable DOF	3	2	3
Applications	Oceanographic Survey; Environmental Monitoring; Intelligence, Surveillance and Reconnaissance; Rapid Environmental Assesment; Harbour and Port Security.		

versatile pieces of robotic data acquisition equipment. The concept of an AUG was proposed by Henry Stommel and Doug Webb in 1989 [4]. A prototype Slocum glider

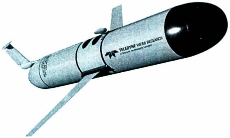

Figure 1.1: Slocum Glider (Image From Teledyne Webb Research)

was fabricated and tested in open-loop shallow water field trials in January 1991 [7]. After ten years' development and improvement, the first underwater glider, named after Joshua Slocum, the first man to sail around the world alone, was developed by Teledyne Webb Research Corporation. Up to the present, 3 commercially available gliders have been developed: the Slocum Underwater Glider (Figure 1.1), the Seaglider (Figure 1.2), and the Spray (Figure 1.3). They are quiet, reliable, effective, and low-cost [34]. Table 1.1 lists the specific details of these three legendary AUGs [8]. Furthermore, the XRay glider (Figure 1.4), a newly designed high-performance AUG, was developed by the Applied Physics Laboratory at the University of Washington cooperating with the Marine Physics Lab at the Scripps Institution of Oceanography, U.S.A.. Due to its hydrodynamic optimization, the XRay Glider can travel at a higher speed than the legacy gliders [5].

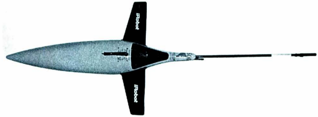

Figure 1.2: Seaglider (Image From iRobot Maritime System)

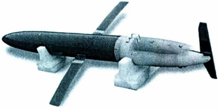

Figure 1.3: Spray Glider by Bluefin Robotics (Image From auvac.org)

AUGs are popular for their easy deployment, energy efficiency and payload sensors integration. Usually, the behaviours of the underwater gliders are determined by the buoyancy engine and pitch battery actuator instead of a conventional propeller and an external control surface based propulsion and control system, which requires continuous power. An unique saw-tooth motion pattern in the vertical plane is generated due to the glide path.

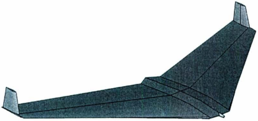

Figure 1.4: XRay Glider Developed by the Applied Physics Laboratory, University of Washington

As shown in Table 1.1, AUGs are capable of long-term missions for weeks, and even months, in depths of over 1000 meters covering hundreds or even thousands of nautical miles. A Trans-Atlantic attempt was undertaken by Rutgers undergraduates using a Slocum underwater glider from March to April, 2008 [13]. Two Slocum gliders were launched from the New Jersey Coast, U.S.A., heading to Halifax, N.S., Canada, a distance of 2600 kilometers. Up to the present, the longest mission (5 months and covering 2700 km) was accomplished by a Seaglider in the Gulf of Alaska and the Labrador Sea [9]. During missions, the glider measured the temperature, current, and other ocean qualities along the water column with the sensors onboard. The measurements obtained by an underwater glider are transmitted remotely by wireless telemetry during the glider's surfacing period. In addition, engineers and scientists can equip AUGs with various sensors to obtain specific data. For instance, the Autonomous Ocean System Laboratory (AOSL) has integrated a single beam, upward looking ice-profiling sonar [11], and an Annderra Oxygen Optode sensor [12], as well as a Microstrain 3DM-GX3-25 Altitude Heading Reference System (AHRS).

1.2 Ice Management

On the east coast of Canada (and particularly off the coast of Newfoundland), the icebergs originating from the glaciers in western Greenland are a major concern for the offshore industry in the Terra Nova and the Hibernia areas. Above sea-level, ice-induced downtime is economically damaging. Meanwhile the deep-keel iceberg, which has a potential of scouring the seafloor, may destroy subsea facilities such as wellheads, risers, and pipelines.

Table 1.2: Iceberg Categories [10]

Shape	Description	Illustration
Tabular	Horizontal or flat-topped with length to height ratio of 5:1 or more	Figure 1.5 A
Blocky	Steep precipitous sides with near horizontal top and length to height ratio of less than 5:1	Figure 1.5 B
Domed	Smooth round top	Figure 1.5 C
Dry Dock	Eroded such that a large U-shaped slot is formed with twin columns or pinnacle slot extends into the water-line or close to it	Figure 1.5 D
Pinnacled	One or more large spires or pyramids dominating overall shape	Figure 1.5 E

Based on the annual report of the International Ice Patrol (IIP) in the North Atlantic [14], 1204 icebergs were detected around Newfoundland and Labrador's coast (North 48^o latitude) in the summer of 2009. Their classification based on the iceberg shape is shown in Table 1.2.

Ice management is always required for all hydrocarbon exploration and development activities by the Canada Newfoundland and Labrador Offshore Petroleum Board (CN-LOPB) [17]. Ice management has been further discussed in [15], [16] and [17], and the role of ice management is briefly summarized:

1. To ensure that the platform operates safely in the environment for which it was

designed;

2. To reduce risk to personnel, the environment and assets over and above design requirements;
3. To minimize disruption to drilling or producing operations.

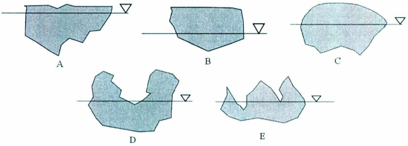

Figure 1.5: The Catergories of Icebergs with Different Shapes [10]

Moreover, the following procedures must be addressed in the ice management plan for oil and gas development [17]:

1. Ice detection and surveillance,
2. Ice data reporting, collation and quality control,
3. Tactical ice forecasting,
4. Iceberg deflection,
5. Response of the installation to ice encroachment.

Ice detection and surveillance are implemented by airborne sensors [18] [19]. Underwater acoustic techniques, optical-based and electromagnetic techniques are used in iceberg data collecting and reporting. Canadian Seabed Research Ltd.[10] summarizes and compares the techniques employed in subsea iceberg draft profiling. In 2003, Oceans Ltd. and the Canadian Hydraulics Centre used a tethered, side scan sonar equipped probe for a 3D underwater profiling of an iceberg[20]. In 2010 the concept of a free-falling, self-rotating, autonomous iceberg-profiling probe equipped with a profiling sonar was proposed[21].

Iceberg deflection techniques are executed based on the iceberg reports. The following iceberg deflection techniques are utilized by the Hibernia Management and Development Company Ltd..

- Single vessel towing
- Dual vessel towing
- Prop wash
- Water cannon

If the deflection technique is not effective, an alternative operation should be conducted to minimize the environmental impact and risk to personnel.

1.3 Problem Statement

1.3.1 The Potential and Challenge of the Slocum Underwater Glider

The Slocum glider available in the AOSL is a buoyancy driven AUV. In the previously conducted mission, the Slocum glider flew with a horizontal velocity of 0.4 m/s and a vertical speed of 0.2 m/s. In a Slocum glider, an electric piston located at the nose of the glider takes in and expels the water within the range of $\pm 250\ cm^3$, which alters the buoyancy of the glider. Moreover, a sliding mass, which is able to translate linearly along the longitudinal direction inside, fine tunes the pitch angle of the Slocum glider. The rudder at the tail is designed to tune the lateral motion.

As mentioned in Section 1.2, iceberg management is neccessary and mandatory for the Atlantic Canada offshore industry. However, the traditional sensors, which are satellite, airborne and vessel based, employed for ice detection, surveillance and assessment, are very costly. For underwater iceberg-profiling, the acoustic underwater profiling approaches mentioned in [10], [20] and [21] are restricted by the maximum sonar profiling range. On the other hand, AUGs, which are easy to deploy, autonomous, and have a long endurance, show the potential to be employed for ice surveillance and data collection. The glider proposed in this thesis can be used for iceberg profiling.

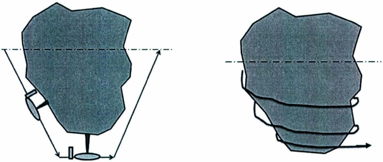

Figure 1.6: Glider Mission(Left: Straight Gliding. Right: Spiral Gliding)

In 2007, the AOSL at Memorial University of Newfoundland (MUN) integrated a single beam, upward looking ice-profiling sonar into the Slocum Underwater Glider. Prior to the integration of this sonar an initial field trial was conducted by MUN in Western Greendland[11] using a modified altimeter already present on the glider. The Slocum glider was programmed to fly in a straight crisscross pattern underneath the target iceberg (Figure 1.6). During the trial, temperature and salinity data were collected along with the underside draft of the iceberg.

Although ordinary straight profiling is a relatively rapid way of measuring the depth of an iceberg, spiral profiling (Figure 1.6) is essential in order to gather an accurate

3D draft of the iceberg. To point the sonar towards the iceberg and to avoid collisions during spiral profiling, the roll angle control becomes significant to the mission.

This thesis focuses on analyzing the 6 Degree of Freedom (DOF) dynamic model of the Slocum glider, and presenting roll control improvement approaches on a Slocum underwater glider.

1.3.2 Vehicle Roll Control Survey

The internal mass shifting mechanism is the most common roll control method in the existing AUV system. In a Seaglider [9], a 16mm Maxon neodymium magnet motor is installed to rotate the battery pack inside the electronics section. The glider rolls due to the misalignment of Center of Buoyancy (CB) and Center of Gravity (CG) in the wingspan direction. Also in the glider built by the National Research Council Institute for Ocean Technology (NRC-IOT) [22], the same mechanism was designed to control the roll angle of the vehicle. Moreover, the roll motion can also be controlled by altering external control surfaces such as wings and rudders. For instance, the orientation of the Explorer AUV is controlled by the X-tail configuration (Figure 1.7). The control surfaces deflect in the same direction to increase the hydrodynamic torque on the vehicle resulting in a rolling moment.

Modern aircraft typically use either ailerons or spoilers to control lateral motions such as rolling and turning. These ailerons and spoilers roll the aircraft by reversing the lift forces on the two wings. In a sophisticated aircraft desgin, the development of new material offers an opportunity for creating a morphing aircraft. In response to the pilot command, the wing geometry can be tailored (altering the wing sweep angle, camber shape, or span length) to alter the aerodynamic performance [24]. The morphing wing aircraft was first discussed by H. F. Parker [25], who intended to increase the forward speed of the aircraft by variating the camber. At the University of Maryland, a Variable Span Morphing Wing (VSMW) was designed and tested as an effector of roll control for unmanned aerial vehicles (UAVs)[24]. Meanwhile, a micro air vehicle with morphing wings was designed at the University of Florida [26]. The performance of the micro air vehicle is summarized in [27]; the effect of wing twisting and curling to the 360^o rolls is examined and evaluated. The flight test shows that wing twisting and curling provide sufficient control of high level roll performance.

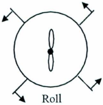

Figure 1.7: Back View of the Explorer X-Tail [23]

1.4 Thesis Outline

Chapter 1

The Autonomous Underwater Vehicles (AUVs) and Autonomous Underwater Gliders (AUGs) are introduced. With the discussed advantages, underwater gliders have shown a potenial to be involved in ice management in the North Atlantic.

Chapter 2

A simplified 6 DOF dynamic model of the Slocum Underwater Glider is presented and validated by comparing the simulation data to the field trial data collected in Conception Bay, Newfoundland, 2010. The model presented in Chapter 2 can be modified to accomodate various customized Slocum glider structures, including other AUVs. In the dynamic model, a trim weight is included to simulate the performance of the Slocum glider in 6 DOF.

Chapter 3

Two roll control mechanisms are introduced and presented. The Autonomous Roll Trimming Mechanism (ARTM) can simplify the tank ballasting process and eliminate the roll angle error. The ARTM can easily be powered on/off mechanically or in software. Additionally, the original wing assembly is replaced by the newly designed Deflectable Wingtip Mechanism (DWM) which is inspired by the morphing aircraft. Based on the mathematical simulation result, the Slocum Underwater Glider is expected to achieve a roll angle of 45^o with a relatively small deflection on the DWM.

Chapter 4

The performance of the DWM is evaluated experimentally for the future integration and control of Slocum glider. A hydrodynamic platform which has 3 rotation freedoms is designed. The DWM is tested in the flume tank at Memorial University of Newfoundland. The hydrodynamic data in 6 DOF with respect to a different angle of attack (AOA), deflection angle and wing sweep angle are recorded by a 3-axis load cell.

Chapter 5

Conclusions and recommendations for future works are discussed in this chapter.

Chapter 2

Mathematical Model for Slocum Underwater Glider

2.1 Modeling Overview

Because of the hydrodynamic complexity and the alignment of the internal masses, the analysis of the dynamics of the AUG is challenging. For example, the motion of a Slocum glider is controlled by a rudder, a buoyancy engine, and an internal linear actuator. Since the understanding of aircraft, aerodynamics and hydrodynamics is well developed, and the underwater glider and aircraft, especially the sailplane, share some characteristics, AUG dynamics can be derived from the aircraft modeling theories. However, the difference between AUGs and the sailplanes has to be considered when applying the aircraft model to the AUG. The significant differences are discussed in [28] and summarized as follows,

1. Underwater gliders have buoyancy altering mechanisms.
2. Stability of AUGs and sailplanes depends on the separation of CG and CB, and aerodynamics respectively.

3. Different gliding path angle. For example, the pitch angle of the Slocum underwater glider is controlled in the range of $\pm 27^o$. On the other hand, the glide path of sailplanes is controlled to maximize the glide slope (the distance traveled for each unit of height lost).

4. Different flight Reynolds number regime. For example, the Slocum glider is operating at the Reynolds number with transitional flow, while the Sailplane is gliding at the Reynolds number with turbulent flow.

For the dynamic model of the aircraft, [29], [30] and [31] thoroughly explain the dynamics of aircraft and applied control theories. Meanwhile, the comprehensive dynamics of underwater vehicles are included in [32] and [33].

The dynamic model of the AUG presented in this chapter summarizes and generalizes the glider model discussed in [28] and [34] - [40]. Based on the existing models, the equations of motions derived in this chapter are simplified with the assumptions:

1. Rigid body assumption,

2. Neglect the movable mass acceleration effects,

3. Uniform symmetric hull (exclude the tail rudder),

4. Diagonal added mass and inertia matrices (no cross term in the added mass and inertia matrices),

5. No external flow.

The following sections establish the Slocum glider based AUG dynamic model. Since underwater gliders are used for a large variety of oceangraphic applications, various sensors are available for integration on AUGs. Therefore, the mass distribution can vary from one glider to another, and each glider needs to be accurately trimmed and ballasted. The advantage of the dynamic model presented in this chapter is that the model is easily modified corresponding to the realistic mass distribution of an AUG helping in the trimming and ballasting process.

2.2 Coordinate Systems and Transformations

In order to describe the glider status conveniently, 3 coordinate systems are assigned. The coordinate systems are assigned based on general marine and aircraft dynamic theory. All the coordinate definitions and transformation of aircraft and marine vehicles are thoroughly discussed in Chapter 4 of [29] and Chapter 2 of [32]. Three coordinate systems: Earth Fixed Coordinate, Body Fixed Coordinate, and Stream Coordinate are introduced in the modeling. They are explained in Table 2.1, and illustrated in Figure 2.1.

Table 2.1: Coordinate Systems

Coordinate Systems	Origin	X Axis	Y Axis	Z Axis
Earth Fixed Coordinate (e1,e2,e3)	Initial deploy point	Initial glider velocity direction in the horizontal plane	Obtained by using right hand thumb rule	Pointing vertically downward
Body Fixed Coordinate (b1,b2,b3)	CB of glider	Longitudinal direction of glider pointing towards nose	Wingspan direction of glider pointing left	Obtained by using right hand thumb rule
Stream Coordinate (w1,w2,w3)	CB of glider	In the opposite direction of drag force	obtained by using right hand thumb rule	in the opposite direction of lift force

The transformation between two coordinates is parameterized by the Euler angles. In our case, the roll angle (ϕ) and pitch angle (θ) are between ± 90 where the Euler angle representation is unique. The yaw angle (ψ) can be relatively large, but it will not affect the transformation (Equation 2.5) between different coordinates. Figure

2.2 shows the top view of the glider. The yaw ψ is defined as positive when the glider rotates clockwise in the top view, pitch θ is positive when the glider is nose-up, and the roll ϕ is positive when the right wing is down.

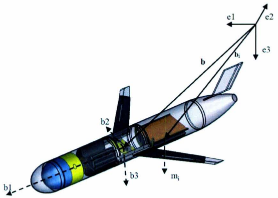

Figure 2.1: Geometric Relationship Between Body Fixed Coordinate and Earth Fixed Coordinate

The Body Fixed Coordinate can be obtained by rotating the Earth Fixed Coordinate according to the following steps as illustrated in 2.3:

1. Align XYZ of the Body Fixed Coordinate with the XYZ in the Earth Fixed Coordinate;
2. XYZ rotates about Z axis with a Yaw ψ angle. XYZ becomes X'Y'Z;
3. X'Y'Z rotates about Y' axis with a Pitch θ angle. X'Y'Z becomes X"Y'Z';
4. X"Y'Z' rotates about X" axis with a Roll ϕ angle. X"Y'Z' becomes X"Y"Z";
5. X"Y"Z" is defined as the Body Fixed Coordinate.

The rotation matrix from Earth Fixed Coordinate to Body Fixed Coordinate consists

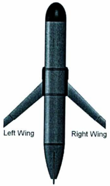

Figure 2.2: Top View of Glider

of 3 parts, that:

$$\mathbf{R}_{EB} = R_\phi R_\theta R_\psi \tag{2.1}$$

where the rotation matrices R_ϕ, R_θ, and R_ψ are shown in Equation 2.2, 2.3 and 2.4.

$$R_\psi = \begin{pmatrix} cos\psi & sin\psi & 0 \\ -sin\psi & cos\psi & 0 \\ 0 & 0 & 1 \end{pmatrix} \tag{2.2}$$

$$R_\theta = \begin{pmatrix} cos\theta & 0 & -sin\theta \\ 0 & 1 & 0 \\ sin\theta & 0 & cos\theta \end{pmatrix} \tag{2.3}$$

$$R_\phi = \begin{pmatrix} 1 & 0 & 0 \\ 0 & cos\phi & sin\phi \\ 0 & -sin\phi & cos\phi \end{pmatrix} \tag{2.4}$$

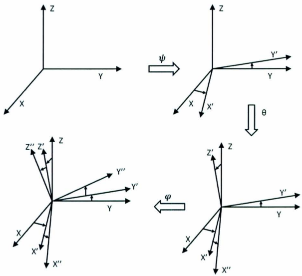

Figure 2.3: Earth Fixed Coordinate to Body Fixed Coordinate Rotation

By multiplying the three matrices, we can obtain the rotation matrix from the Earth Fixed Coordinate to the Body Fixed Coordinate (See Equation 2.5). Meanwhile, the rotation matrix from the Body Fixed Coordinate to the Earth Fixed Coordinate (R_{BE}) which is equal to ${R_{EB}}^T$, can be obtained.

$$\mathbf{R}_{EB} = \begin{pmatrix} cos\psi cos\theta & sin\psi cos\theta & -sin\theta \\ -sin\psi cos\theta + cos\psi sin\theta sin\phi & cos\psi cos\theta + sin\phi sin\theta sin\psi & cos\theta sin\phi \\ sin\psi sin\phi + cos\psi cos\phi sin\theta & -cos\psi sin\phi + sin\theta sin\psi cos\phi & cos\theta cos\phi \end{pmatrix} \tag{2.5}$$

In addition, the hydrodynamic forces and torques are represented in the Stream Coordinate. To describe the Stream Coordinate, the angle of attack (α) and the sideslip angle (β) are defined in the Body Fixed Coordinate and the expression of α and β are shown in Equation 2.6, where we define $\boldsymbol{v} = (u, v, w)^T$ is the translational velocity of the vehicle in the body fixed coordinate.

$$\alpha = atan2(w, u) \qquad and \qquad \beta = atan2(v, \sqrt{u^2 + v^2 + w^2}) \tag{2.6}$$

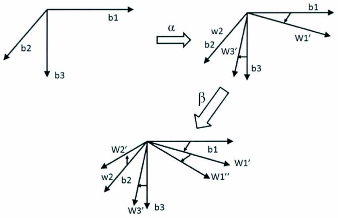

Figure 2.4: Body Fixed Coordinate to Stream Coordinate

The Stream Coordinate is obtained by rotating the Body Fixed Coordinate as follows (see Figure 2.4),

1. the Stream Coordinate aligns with Body Fixed Coordinate,
2. the wind axes rotate about w2 with an angle of α,
3. the wind axes rotate about w3 with an angle of β.

The rotation matrices in the steps mentioned above are described in Equation 2.7 and Equation 2.8. Similar to the $\boldsymbol{R}_{EB}$, the rotation matrix (Equation 2.9) from Body Fixed Coordinate to Stream Coordinate is obtained by multiplying R_β and R_α. We also have $\mathbf{R}_{WB} = \mathbf{R}_{BW}{}^{T}$

$$R_\alpha = \begin{pmatrix} cos\alpha & 0 & sin\alpha \\ 0 & 1 & 0 \\ -sin\alpha & 0 & cos\alpha \end{pmatrix} \tag{2.7}$$

$$R_\beta = \begin{pmatrix} cos\beta & sin\beta & 0 \\ -sin\beta & cos\beta & 0 \\ 0 & 0 & 1 \end{pmatrix} \tag{2.8}$$

$$\mathbf{R}_{BW} = R_\beta R_\alpha = \begin{pmatrix} cos\alpha cos\beta & sin\beta & sin\alpha cos\beta \\ -cos\alpha sin\beta & cos\beta & -sin\alpha sin\beta \\ -sin\alpha & 0 & cos\alpha \end{pmatrix} \tag{2.9}$$

2.3 Mass Distribution

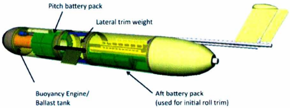

Figure 2.5: Mass Distribution Inside a Glider (Image by Christian Knapp/ NRC-IOT)

Figure 2.5 shows the internal arrangement of the Slocum glider. Basically, the motion of the Slocum glider is executed by altering the internal mass distribution and the buoyancy. In the downward motion, the ballast tank weight is increased by taking in water. In the opposite direction, the ballast tank expels the water. The Slocum glider is only capable of controlling 3 DOF (X, Z and pitching) in the vertical plane.

In the horizontal plane, the heading of the vehicle is currently controlled by the rudder. However, the rudder will induce an additional drag and affect the roll trim ballasting. Thus, we introduced a lateral trim mass in the mathematical model, which helps the development of the glider's performance in 6 DOF. The trim mass is an additional mass which is movable in the b2 direction in the Body Fixed Coordinate. By adding the trim mass, we can explore the 6 DOF motions such as banked-turn and downward/upward spiraling. The masses (stationary mass, offset mass, and movable mass), included in the dynamic model are categorized in Table 2.2.

Table 2.2: Masses Included in the Dynamic Model

Masses	Annotation	Category	Weight[kg]	Location[cm]		
				b1	b2	b3
Hull	m_h	Stationary	34	0	0	0
Ballast Tank	m_b	Offset	[-0.25, 0.25]	71	0	0
Aft. Battery	m_{bb}	Offset	7.6	-34.4	0	6.5
Pitch Battery	m_{pb}	Movable Mass	9.4	[26.7, 28.7]	0	0
Trim Mass	m_t	Movable Mass	1	0	[-6, 6]	0

Note: The location [a, b] defines the movable range of a mass

2.4 Kinematic Equation

The Kinematic Equation represents the transformation between coordinate systems. In the Earth Fixed Coordinate, $\mathbf{b}=(X, Y, Z)^T$ represents the displacement of the glider, and $\boldsymbol{\Omega} = (\dot{\phi}, \dot{\theta}, \dot{\psi})^T$ is the angular velocity of the glider. Meanwhile, we define $\boldsymbol{v} = (u, v, w)^T$ and $\boldsymbol{\omega} = (p, q, r)^T$ as the translation velocity and angular velocity of the glider in the Body Fixed Coordinate.

As discussed in Section 2.2, the linear velocity and angular velocity in the Body Fixed Coordinate and Earth Fixed Coordinate can be converted to each other by using the transformation matrices mentioned. Thus, the mathematical relation of the motion of the glider between the Earth Fixed Coordinate and the Body Fixed Coordinate are expressed in Equation 2.10 to Equation 2.12.

$$\dot{\boldsymbol{b}} = \mathbf{R}_{EB}{}^{T} \cdot \boldsymbol{v} \tag{2.10}$$

$$\boldsymbol{\omega} = \begin{pmatrix} p \\ q \\ r \end{pmatrix} = \begin{pmatrix} \dot{\phi} \\ 0 \\ 0 \end{pmatrix} + R_{\phi} \begin{pmatrix} 0 \\ \dot{\theta} \\ 0 \end{pmatrix} + R_{\phi} R_{\theta} \begin{pmatrix} 0 \\ 0 \\ \dot{\psi} \end{pmatrix} \tag{2.11}$$

$$= \begin{pmatrix} \dot{\theta} - \dot{\psi} sin\theta \\ \dot{\theta} cos\phi + \dot{\psi} cos\theta sin\phi \\ -\dot{\theta} sin\phi + \dot{\psi} cos\theta cos\phi \end{pmatrix} = \begin{pmatrix} 1 & 0 & -sin\theta \\ 0 & cos\phi & cos\theta sin\phi \\ 0 & -sin\phi & cos\theta cos\phi \end{pmatrix} \begin{pmatrix} \dot{\phi} \\ \dot{\theta} \\ \dot{\psi} \end{pmatrix} \tag{2.12}$$

To sum up, based on the orientation of the Body Fixed Coordinate to the Earth Fixed Coordinate, we obtained the transformation of the translation and angular velocities in the Body Fixed Coordinate and Earth Fixed Coordinate (Equation 2.13 and Equation 2.14).

$$\begin{pmatrix} \dot{X} \\ \dot{Y} \\ \dot{Z} \end{pmatrix} = \mathbf{R}_{EB}{}^{T} \cdot \begin{pmatrix} u \\ v \\ w \end{pmatrix} \tag{2.13}$$

$$\begin{pmatrix} \dot{\phi} \\ \dot{\theta} \\ \dot{\psi} \end{pmatrix} = \begin{pmatrix} 1 & 0 & -sin\theta \\ 0 & cos\phi & cos\theta sin\phi \\ 0 & -sin\phi & cos\theta cos\phi \end{pmatrix}^{-1} \begin{pmatrix} p \\ q \\ r \end{pmatrix} \tag{2.14}$$

2.5 Dynamic Equation

In this section the dynamic equation is developed based on Newton's second law (Equation 2.15 and 2.16) which is also used in aircraft modeling in [41]. This means the changes of momentum are due to the accumulated external force and torque.

$$\mathbf{m} \cdot \dot{\boldsymbol{v}} = \sum \mathbf{F} \tag{2.15}$$

$$\mathbf{J} \cdot \dot{\boldsymbol{\omega}} = \sum \mathbf{T} \tag{2.16}$$

Moreover, the cross product operator $\hat{\boldsymbol{x}}$ (Equation 2.19) is used to simplify matrix calculations. For example $\mathbf{x} = (x_1, x_2, x_3)^T$ and $\mathbf{y} = (y_1, y_2, y_3)^T$

$$\mathbf{x} \times \mathbf{y} = \begin{pmatrix} \mathbf{i} & \mathbf{j} & \mathbf{k} \\ x_1 & x_2 & x_3 \\ y_1 & y_2 & y_3 \end{pmatrix} = \mathbf{i}(x_2 y_3 - x_3 y_2) + \mathbf{j}(x_3 y_1 - x_1 y_3) + \mathbf{k}(x_1 y_2 - x_2 y_1) \tag{2.17}$$

$$= \begin{pmatrix} x_2 y_3 - x_3 y_2 \\ x_3 y_1 - x_1 y_3 \\ x_1 y_2 - x_2 y_1 \end{pmatrix} = \begin{pmatrix} 0 & -x_3 & x_2 \\ x_3 & 0 & -x_1 \\ -x_2 & x_1 & 0 \end{pmatrix} \begin{pmatrix} y_1 \\ y_2 \\ y_3 \end{pmatrix} \tag{2.18}$$

Therefore, the cross product operator is defined so that

$$\hat{\mathbf{x}} = \begin{pmatrix} 0 & -x_3 & x_2 \\ x_3 & 0 & -x_1 \\ -x_2 & x_1 & 0 \end{pmatrix} \tag{2.19}$$

and

$$\mathbf{x} \times \mathbf{y} = \hat{\boldsymbol{x}}\mathbf{y} \tag{2.20}$$

2.5.1 Inertia Terms

Equation 2.15 and Equation 2.16 are combined in Equation 2.21,

$$\begin{pmatrix} \dot{\boldsymbol{v}} \\ \dot{\boldsymbol{\omega}} \end{pmatrix} = \mathbb{I}^{-1} \begin{pmatrix} \dot{\boldsymbol{P}} \\ \dot{\boldsymbol{L}} \end{pmatrix} \tag{2.21}$$

where $\mathbf{P}$ and $\mathbf{L}$ are the linear momentum and angular momentum respectively, and $\mathbb{I}$ is a 6×6 inertia matrix shown in Equation 2.22.

$$\mathbb{I}_{6\times 6} = \begin{pmatrix} \mathbf{M}_{3\times 3} & \mathbf{C}_{3\times 3} \\ \mathbf{D}_{3\times 3} & \mathbf{J}_{3\times 3} \end{pmatrix} \tag{2.22}$$

where $\mathbf{M}_{3\times 3}$ is the mass matrix of the vehicle including added mass matrix ($\mathbf{M}_{added}$), and all the masses on the vehicle. $\mathbf{J}_{3\times 3}$ is the momentum of inertia including the added moment of inertia ($\mathbf{J}_{added}$), and the momentum of inertia of the masses on the vehicle. $\mathbf{C}_{3\times 3}$ and $\mathbf{D}_{3\times 3}$ are the cross term matrices which only include the cross term effects of the offset masses and movable masses, because of the assumption of the no cross term in the added mass and inertia matrices. The glider is operating at low angle of attack. The hydrodynamic effect is dominated by the lift and drag force. Therefore, the added mass and added inertia can be assumed diagonal.

Based on the general rigid body dynamics discussed in[42] and [43], the linear momentum cross term created by the rotation of an offset mass (m) can be calculated by using Equation 2.23.

$$\mathbf{P}_m = m \cdot \boldsymbol{v} = m\boldsymbol{\omega} \times \mathbf{r} = -m\mathbf{r} \times \boldsymbol{\omega} = -m\hat{\mathbf{r}}\boldsymbol{\omega} \tag{2.23}$$

Similarly, the angular momentum cross term created by the linear motion of an offset mass (m) can be obtained in Equation 2.24.

$$\mathbf{L}_m = \mathbf{r} \times \mathbf{P} = \mathbf{r} \times (m\boldsymbol{v}) = m\mathbf{r} \times \boldsymbol{v} = m\hat{\mathbf{r}}\boldsymbol{v} \tag{2.24}$$

Thus, the cross matrices in the body inertia matrix $\mathbb{I}$ are obtained in Equation 2.25 and Equation 2.26.

$$\mathbf{C}_{3\times3} = -\sum m_{offset}\hat{\mathbf{r}}_{offset} - \sum m_{movable}\hat{\mathbf{r}}_{movable} \tag{2.25}$$

$$\mathbf{D}_{3\times3} = \sum m_{offset}\hat{\mathbf{r}}_{offset} + \sum m_{movable}\hat{\mathbf{r}}_{movable} \tag{2.26}$$

Furthermore, the offset masses and movable masses create additional moments of inertia in the moment of inertia matrix ($\mathbf{J}_{3\times3}$). The moment of inertia of an offset mass (m) is expressed as follows,

$$\mathbf{L}_J = \mathbf{r} \times \mathbf{P} = \mathbf{r} \times m\boldsymbol{v} = m\mathbf{r} \times \boldsymbol{v} \tag{2.27}$$

$$= m\mathbf{r} \times (\boldsymbol{\omega} \times \mathbf{r}) \tag{2.28}$$

$$= -m\mathbf{r} \times (\mathbf{r} \times \boldsymbol{\omega}) = -m \cdot \hat{\mathbf{r}} \cdot \hat{\mathbf{r}} \cdot \boldsymbol{\omega} \tag{2.29}$$

Therefore, the angular momentum of inertia of the offset and movable masses can be calculated by using Equation 2.27, and $\mathbf{J}_{3\times3}$ in Equation 2.22 becomes:

$$\mathbf{J}_{3\times3} = \mathbf{J}_s + \mathbf{J}_{added} - \sum m_{offset} \cdot \hat{\mathbf{r}}_{offset} \cdot \hat{\mathbf{r}}_{offset} - \sum m_{movable} \cdot \hat{\mathbf{r}}_{movable} \cdot \hat{\mathbf{r}}_{movable} \tag{2.30}$$

The mass matrix ($\mathbf{M}_{3\times3}$) in Equation 2.22 is shown in Equation 2.31.

$$\mathbf{M}_{3\times3} = (\sum m_s + \sum m_{offset} + \sum m_{movable})\mathbf{I}_{3\times3} + \mathbf{M}_{added} \tag{2.31}$$

where $\mathbf{J}_s$ is the moment of inertia of the stationary mass (m_s).

2.5.2 Momentum Terms

After all the inertia matrices in Equation 2.22 are well expressed, the expressions of the angular momentum and the linear momentum of the gliders are developed in this section.

Firstly, the transformation of momentums between Earth Fixed Coordinate and Body Fixed Coordinate is shown in Equation 2.32 and Equation 2.33,

$$\boldsymbol{p} = \mathbf{R}_{BE}\mathbf{P} \tag{2.32}$$

$$\boldsymbol{l} = \mathbf{R}_{BE}\mathbf{L} + \mathbf{b} \times \mathbf{p} \tag{2.33}$$

$$\dot{\boldsymbol{p}} = \mathbf{R}_{BE}\dot{\mathbf{P}} + \mathbf{R}_{BE}\hat{\boldsymbol{\omega}}\mathbf{P} = \boldsymbol{f}_{ext} + \sum \boldsymbol{f}_{gi} \tag{2.34}$$

$$\dot{\boldsymbol{l}} = \mathbf{R}_{BE}\dot{\mathbf{L}} + \mathbf{R}_{BE}\hat{\boldsymbol{\omega}}\mathbf{L} + \mathbf{R}_{BE}\boldsymbol{v} \times \mathbf{P} + \mathbf{b} \times \mathbf{P} = \mathbf{t}_{ext} + \sum_{i=1}^{n}(\mathbf{b}_i \times \boldsymbol{f}_{gi}) \tag{2.35}$$

Equation 2.34 and Equation 2.35 are obtained by differentiating Equation 2.32 and Equation 2.33. The differentiation rules are defined in [43], and Equation 2.10. In the equations, $\boldsymbol{f}_{ext}$ and $\boldsymbol{t}_{ext}$ are the expressions of hydrodynamic forces and torques in the Earth Fixed Coordinate, and $\boldsymbol{f}_{gi}$ is the gravitational force of a mass m_i; for example the hull mass, movable masses, and offset masses in the Earth Fixed Coordinate. Because the gravitational and hydrodynamic forces are acting on the vehicle which is offset from the origin of the Earth Fixed Coordinate, both of them create additional torques,

referring to the origin of the Earth Fixed Coordinate in Equation 2.35. To sum up, in addition to the hydrodynamic torque, the torques created by the hydrodynamic forces and gravitational forces also influence the angular momentum rate. In Equation 2.35, $\sum_{i=1}^{n} \mathbf{b}_i \times \boldsymbol{f}_{gi}$ represents the total gravitational forces created torques, and the hydrodynamic forces created torques are merged into the $\mathbf{t}_{ext}$.
Rearranging the terms in Equation 2.34 and Equation 2.35, we can obtain the rate of change of the linear and the angular momentum in the Body Fixed Coordinate, that:

$$\dot{\mathbf{P}} = \mathbf{P} \times \boldsymbol{\omega} + \mathbf{R}_{EB}\dot{\boldsymbol{p}} = \mathbf{P} \times \boldsymbol{\omega} + m_0 g \mathbf{R}_{EB}\mathbf{k} + \mathbf{R}_{WB}\mathbf{F}_{ext} \tag{2.36}$$

$$\dot{\mathbf{L}} = \mathbf{L} \times \boldsymbol{\omega} - \hat{\boldsymbol{v}}\mathbf{P} + \mathbf{R}_{EB}(-\mathbf{b} \times \dot{\boldsymbol{p}} + \dot{\boldsymbol{l}}) \tag{2.37}$$

When $\dot{\boldsymbol{p}}$ and $\dot{\boldsymbol{l}}$ are replaced with Equation 2.34 and Equation 2.35, Equation 2.37 becomes:

$$\dot{\mathbf{L}} = \mathbf{L} \times \boldsymbol{\omega} - \hat{\boldsymbol{v}}\mathbf{P} + \mathbf{R}_{EB}(\sum_{i=1}^{n} (\mathbf{b}_i - \mathbf{b}) \times \boldsymbol{f}_{gi} + \mathbf{t}_{ext}) \tag{2.38}$$

In Figure 2.6, $\mathbf{b}_i$ is the displacement of m_i in the Earth Fixed Coordinate, while $\mathbf{b}$ is the displacement of the origin of the Body Fixed Coordinate in the Earth Fixed Coordinate. Therefore, $\mathbf{b}_i - \mathbf{b}$ represents the displacement of m_i in the Body Fixed Coordinate, and $(\mathbf{b}_i - \mathbf{b}) \times \boldsymbol{f}_{gi}$ represents the torque created by the gravitational forces of m_i referring to the origin of the Body Fixed Coordinate. Consequently, Equation 2.38 becomes:

$$\dot{\mathbf{L}} = \mathbf{L} \times \boldsymbol{\omega} - \hat{\boldsymbol{v}}\mathbf{P} + (\sum m_{offset}\mathbf{r}_{offset} + \sum m_{movablet}\mathbf{r}_{movable}) \times g\mathbf{R}_{EB}\mathbf{k} + \mathbf{R}_{WB}\mathbf{T}_{ext} \tag{2.39}$$

where $\mathbf{F}_{ext}$ and $\mathbf{T}_{ext}$ represent the hydrodynamic forces and torques in the Body Fixed Coordinate.
Moreover, the linear momentum $\mathbf{P}$ (Equation 2.40) and angular momentum $\mathbf{L}$ (Equa-

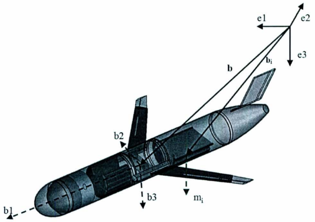

Figure 2.6: The Relation of the Position of a Mass in Earth Fixed Coordinate and Body Fixed Coordinate

tion 2.41) in the Body Fixed Coordinate are obtained so that:

$$\mathbf{P} = \mathbf{M}_{added} \cdot \boldsymbol{v} + \sum m_s \boldsymbol{v} + \sum m_{offset}(\boldsymbol{v} + \hat{\boldsymbol{\omega}}\mathbf{r}_{offset}) + \sum m_{movable}(\boldsymbol{v} + \hat{\boldsymbol{\omega}}\mathbf{r}_{movable}) \tag{2.40}$$

$$\mathbf{L} = \mathbf{J}_{added}\boldsymbol{\omega} + \sum m_s \boldsymbol{\omega} + \sum m_{offset}\hat{\mathbf{r}}_{offset}(\boldsymbol{v} + \hat{\boldsymbol{\omega}}\mathbf{r}_{offset}) + \sum m_{movable}\hat{\mathbf{r}}_{movable}(\boldsymbol{v} + \hat{\boldsymbol{\omega}}\mathbf{r}_{movable}) \tag{2.41}$$

Thus, $\dot{\mathbf{P}}$ and $\dot{\mathbf{L}}$ can be solved by replacing $\mathbf{P}$ and $\mathbf{L}$ in Equation 2.36 and 2.39.

2.5.3 Hydrodynamic Terms

In [35], the author provides the coefficient based hydrodynamic forces and torques expressions (Equation 2.42 - Equation 2.47). Similar to aerodynamic modelling, the coefficients are estimated in referencing to [44] by using the data for generic aerodynamic bodies, then validated by the wind tunnel experiment in [45] or the parameter identification techniques in [46]. Furthermore, in [28] and [49], the hydrodynamic coefficients are obtained from the experiment in the sea. The added mass and added inertia (Equation 2.48 and 2.49) are calculated by using hydrodynamics theory in [47] and [48], and exclude the added mass and inertia of the wings and the tail [35]. Also in [50] Computational Fluid Dynamics(CFD) is used to analyze the added mass and added inertia of the underwater vehicle, such as the Slocum glider and XRay glider. All the hydrodynamic coefficients (Table 2.3) included in our model are obtained based on [35]. However, besides using the lift and drag coefficients published in [35] a separate calibration of lift and drag forces has been done using the steady state value of the glider for horizontal velocity and vertical velocity. After the calibration, the translational velocity decreases to 0.55 m/s which is more realistic.

Table 2.3: Hydrodynamic Coefficient in the Simulation[35]

Coefficient		Coefficient		Coefficient	
K_{D0}	3.4 kg/m	K_{q1}	-20 kg.s/rad^2	m_{f1}	5 kg
K_D	45 kg/m/rad^2	K_{q2}	-60 kg.s/rad^2	m_{f2}	60 kg
K_β	20 kg/m/rad	K_{q3}	-20 kg.s/rad^2	m_{f3}	70 kg
K_{L0}	0 kg/m	K_{M0}	0kg	J_{f1}	4 kg.m^2
K_L	260 kg/m/rad	K_M	-50 kg/rad	J_{f2}	12 kg.m^2
K_{MR}	-60 kg/rad	K_{MY}	100 kg/rad	J_{f3}	11 kg.m^2

$$D = (K_{D0} + K_D\alpha^2)V^2 \tag{2.42}$$

$$SF = K_\beta \beta V^2 \tag{2.43}$$

$$L = (K_{L0} + K_L\alpha)V^2 \tag{2.44}$$

$$M_{DL1} = K_{MR}\beta V^2 + K_{q1}pV^2 \tag{2.45}$$

$$M_{DL2} = (K_{M0} + K_M\alpha + K_{q2}q)V^2 \tag{2.46}$$

$$M_{DL3} = K_{MY}\beta V^2 + K_{q3} r V^2 \tag{2.47}$$

$$\mathbf{M}_{added} = \begin{pmatrix} m_{f1} & 0 & 0 \\ 0 & m_{f2} & 0 \\ 0 & 0 & m_{f3} \end{pmatrix} \tag{2.48}$$

$$\mathbf{J}_{added} = \begin{pmatrix} J_{f1} & 0 & 0 \\ 0 & J_{f2} & 0 \\ 0 & 0 & J_{f3} \end{pmatrix} \tag{2.49}$$

2.5.4 Dynamic Equation Summary

All the terms in the dynamic model based on the Newton's second law are developed. In this section, all the expressions of terms and matrices are summarized as follows:

$$\dot{\boldsymbol{v}} = \begin{pmatrix} \dot{u} \\ \dot{v} \\ \dot{w} \end{pmatrix} \tag{2.50}$$

$$\dot{\boldsymbol{\omega}} = \begin{pmatrix} \dot{p} \\ \dot{q} \\ \dot{r} \end{pmatrix} \tag{2.51}$$

$$\mathbb{I} = \begin{pmatrix} \mathbf{M}_{3\times3} & \mathbf{C}_{3\times3} \\ \mathbf{D}_{3\times3} & \mathbf{J}_{3\times3} \end{pmatrix} \tag{2.52}$$

$$\mathbf{M}_{3\times3} = (\sum m_s + \sum m_{offset} + \sum m_{movable})\mathbf{I}_{3\times3} + \mathbf{M}_{added} \tag{2.53}$$

$$\mathbf{C}_{3\times3} = -\sum m_{offset}\hat{\mathbf{r}}_{offset} - \sum m_{movable}\hat{\mathbf{r}}_{movable} \tag{2.54}$$

$$\mathbf{D}_{3\times3} = \sum m_{offset}\hat{\mathbf{r}}_{offset} + \sum m_{movable}\hat{\mathbf{r}}_{movable} \tag{2.55}$$

$$\mathbf{J}_{3\times3} = \mathbf{J}_s + \mathbf{J}_{added} - \sum m_{offset} \cdot \hat{\mathbf{r}}_{offset} \cdot \hat{\mathbf{r}}_{offset} - \sum m_{movable} \cdot \hat{\mathbf{r}}_{movable} \cdot \hat{\mathbf{r}}_{movable} \quad (2.56)$$

$$\dot{\mathbf{P}} = [\mathbf{M}_{added} \cdot \boldsymbol{v} + \sum m_s \boldsymbol{v} + \sum m_{offset}(\boldsymbol{v} + \hat{\boldsymbol{\omega}}\mathbf{r}_{offset}) + \sum m_{movable}(\boldsymbol{v} + \hat{\boldsymbol{\omega}}\mathbf{r}_{movable})] \times \boldsymbol{\omega}$$

$$+ m_0 g \mathbf{R}_{EB}\mathbf{k} + \mathbf{R}_{WB}\mathbf{F}_{ext} \quad (2.57)$$

$$\dot{\mathbf{L}} = [\mathbf{L} = \mathbf{J}_{added}\boldsymbol{\omega} + \sum m_s \boldsymbol{\omega} + \sum m_{offset}\hat{\mathbf{r}}_{offset}(\boldsymbol{v} + \hat{\boldsymbol{\omega}}\mathbf{r}_{offset})] \times \boldsymbol{\omega}$$

$$-\hat{\boldsymbol{v}}[\mathbf{M}_{added} \cdot \boldsymbol{v} + \sum m_s \boldsymbol{v} + \sum m_{offset}(\boldsymbol{v} + \hat{\boldsymbol{\omega}}\mathbf{r}_{offset}) + \sum m_{movable}(\boldsymbol{v} + \hat{\boldsymbol{\omega}}\mathbf{r}_{movable})]$$

$$+(\sum m_{offset}\mathbf{r}_{offset} + \sum m_{movablet}\mathbf{r}_{movable}) \times g\mathbf{R}_{EB}\mathbf{k} + \mathbf{R}_{WB}\mathbf{T}_{ext} \quad (2.58)$$

2.6 Comparing Simulation Result with Field Trial Data

In this section, one downward-upward motion is simulated by using the model stated previously. The dynamic model is evaluated by comparing the simulation result to the field trial data obtained in October 2010 in Conception Bay, NL, Canada.

Table 2.4: Initial States Defined in Simulations

States	Definition	Value	States	Definition	Value
X	Displacement in X	0 m	ϕ	Roll Angle	0^o
Y	Displacement in Y	0 m	θ	Pitch Angle	5^o
Z	Displacement in Z	0 m	ψ	Yaw Angle	0^o
u	Surge Velocity	0.4 m/s	p	Roll Velocity	0 rad/s
v	SwayVelocity	0 m/s	q	Pitch Velocity	0 rad/s
w	Heave Velocity	0 m/s	r	Yaw Velocity	0 rad/s

The simulation modeled the glider motion for a total duration of 848 seconds during which the downward and upward gliding lasted for 424 seconds each. The initial states used for all the simulations in this thesis are listed in Table 2.4. The downward-upward

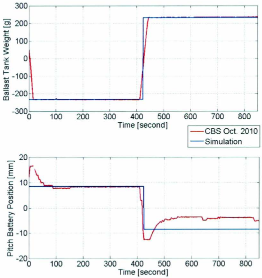

Figure 2.7: Ballast Tank Weight and Pitch Battery Position in 2D Simulation

gliding with the same time period is extracted from the data collected in the field trial at Conception Bay, October 2010. Figure 2.7 shows the status of the actuators in the downward-upward period. The status of actuators in the simulation are assigned as similarly as possible to the control parameters in the field trial: the ballast tank is offset with the same value and the same time period as in the field trial; the pitch battery in the simulation is set at 8.5 mm in the downward and -8.5 mm in the upward motion; and the trim weight remains at zero.

Figure 2.8 shows the comparison of the significant performance parameters (Roll, Pitch, Depth, and Vertical Speed) between the simulation and the mission data. The steady state values such as translation velocity and angle of attack in the simulation are further listed in Table 2.5. The errors between simulation and field trial are discussed below.

Table 2.5: 2D Simulation Steady State Values

Status	Downward	Upward	Status	Downward	Upward
u	54.7 cm/s	54.7 cm/s	θ	-25.2^o	25.2^o
w	1.4 cm/s	-1.4cm/s	α	1.5^o	-1.5^o
$\dot{x}$	48.9 cm/s	48.9 cm/s	$\dot{Z}$	24.6 cm/s	-24.6 cm/s

1. Depth error in Figure 2.8. The main reason causing the depth error is the ballast actuator delay effect, with which the vertical travel distance is less upward than downward. In Figure 2.7 the ballast actuator in the field trial switched from negative to postive with a slope. However, we neglected the ballast actuator delay in the simulation, ie., that the weight of the ballast tank jumps from negative to positive instantanously.

2. Asymmetric pitch battery offset between up and down cast is shown in Figure 2.7. The pitch battery is attached to a lead screw and driven back and forward by a DC motor under a closed-loop position control. In the field trial, it is observed that the position of the pitch battery is asymmetric between upwards and downwards flight, which can be caused by the following effects. 1) Inaccurate ballasting and trimming in the longitudinal direction before the mission, resulting in a small axial misalignment of CG and CB. As a consequence, in order to maintain the same desired pitch angle, the pitch battery position will be different between climbing and diving. 2) The presented model assumed a perfectly symmetric hydrodynamic shape of the glider. However, in reality the glider has protrusions and extensions that will cause asymmetric hydrodynamic effects, i.e. rudder and external sensors. Possibly resulting in asymmetric diving and climbing influence to be compensated by the pitch battery.

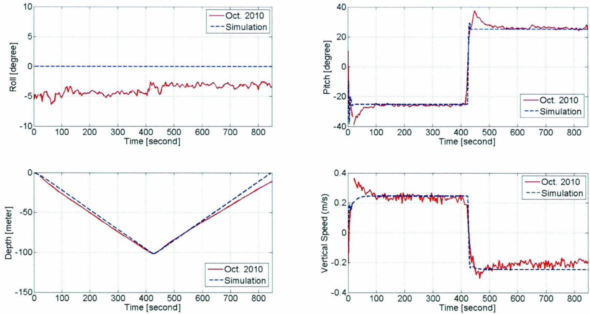

Figure 2.8: 2D Simulation Result Vs. Field Trial

3. Roll angle error in Figure 2.8. The roll angle error between the simulation and field trial is caused by the CG-CB separation in the wingspan direction. Unlike the realistic situation, the CG and CB are not separated in the b2 direction in the simulation.

4. Steady state value error in Table 2.5. The errors are caused by the difference between estimated hydrodynamic coefficients and the in-mission hydrodynamic performance. For example, ocean currents will influence the velocity of the glider.

2.7 3D Performance Simulation Example

After comparing the 2D simulation result with the field trial data, the model has been proved to be relatively accurate in predicting the Slocum glider motion with control parameters (ballast tank weight, pitching battery position) included. In this section, the lateral trim weight defined in the dynamic model is activated to explore the 6 DOF performance of the glider.

The control parameters in the simulation are shown in Figure 2.9: the pitching battery moved forward and backward with an 8 mm offsetting in the diving and climbing respectively; the ballast tank took in 233cc water and expelled 233cc water corresponding to the neutrally buoyant in the diving and climbing; and the trim weight was activated and offset in the b2 direction with a constant distance of 8 cm.

As a result, Figure 2.10 shows the 3 dimensional glider path, and the lateral performance of the glider is illustrated in Figure 2.11. The Slocum glider spiralled downward with a radius of 48 meters and roll angle of 7^o, and ascended with a radius of 36 meters and roll angle of 10^o. Other 3D steady state dynamic performances are further listed in Table 2.6. By observing the simulation result, we found:

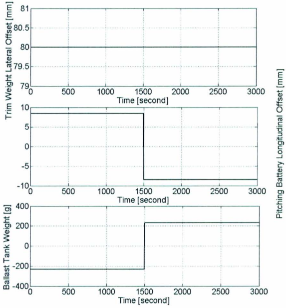

Figure 2.9: Control Parameters Setup in 3D Simulation

1. The Slocum glider is spiraling in different directions in diving and climbing. As introduced, Slocum gliders are buoyancy driven AUVs. The underwater performance of a glider highly depends on the hydrodynamic forces and torques. Figure 2.12 shows the forces (hydrodynamic forces and net weight forces) on the Slocum glider during diving and climbing. In the diving, the net weight points downward, and the combination of hydrodynamic forces tilts left. While climbing, the net weight points upward and hydrodynamic forces tilt right. Thus, the centripetal force which controls the spiraling direction reverses.

2. The Slocum glider is spiraling with a different radius and roll angle in diving and climbing. As listed in the Table 2.6, the β related to the spiraling direction reversed while the roll velocity (p) remained in the same direction diving and

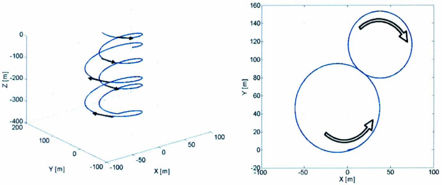

Figure 2.10: Glider Displacement (3D Path and Top View Path) in 3D Simulation

climbing. Consequently, the two components in the M_{DL1} (Equation 2.45) are added together while diving, while substracted from each other while climbing. Therefore the roll angle controlled by the M_{DL1} varied.

3. Damping exists for about 150 seconds at the diving-climbing transition. In the diving/climbing transition, the fast altering of the β (sideslip angle) and α (angle of attack) caused by the altering of the ballast tank and pitch battery breaks the steady state of the glider and causes the variation of hydrodynamic forces and torque. Because we excluded the wing damping effect, M_{DL1} becomes the main factor affecting the roll motion. A long period of damping is observed, and it starts when the ballast tank state jumps. As shown in Table 2.6 the M_{DL1} is smaller in the climbing, resulting in the settling time significantly increasing in the climbing compared to the diving.

The 3D simulation proved the potential of activating the roll motion on the Slocum glider by adding a trim weight movable in the wingspan direction. The dynamic model mentioned in Chapter 2 can be used to predict the Slocum glider performance in both

2D and 3D. Since the simulation shows the potential of expanding the manoeuvrablity of the Slocum glider into 6 DOF, the roll control strategies are discussed and evaluated in the following chapters.

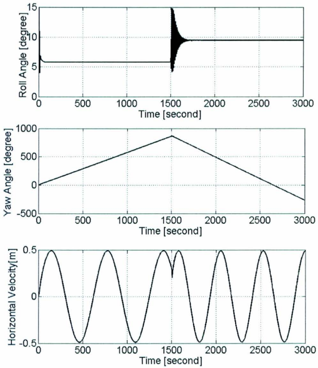

Figure 2.11: Lateral Performance of Glider in 3D Simulation

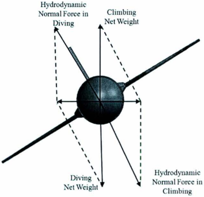

Figure 2.12: The Front View of the Slocum Glider

Table 2.6: 3D Simulation Steady State Values

Status	Definition	Downward	Upward
ϕ	Roll	5.8^o	9.5^o
θ	Pitch	-25.3^o	25.2^o
u	b1 velocity	54.9 cm/s	54.7 cm/s
v	b2 velocity	0.72 cm/s	-0.18 cm/s
w	b3 velocity	1.44 cm/s	-1.46 cm/s
D	Drag	1.11 N	1.11 N
SF	Side force	0.08 N	-0.02 N
L	Lift	1.07 N	-1.08 N
p	Roll velocity	0.0042 rad/s	0.0056 rad/s
q	Pitch velocity	0.0010rad/s	-0.0020rad/s
r	Yaw velocity	0.010 rad/s	-0.012 rad/s
α	Angle of attack	1.50^o	-1.53^o
β	Sideslip angle	0.75^o	-0.19^o
M_{DL1}	Added roll inertia	-0.26 N.m	0.025 N.m
M_{DL2}	Added pitch inertia	-0.41 N.m	0.43 N.m
M_{DL3}	Added yaw inertia	0.34 N.m	-0.027 N.m

Chapter 3

Active Roll Control Approaches

As shown in Chapter 2, the Slocum glider is capable of moving in 6 DOF after roll motion is activated. The simplest way to expand the motion of the glider is to control the roll motion on the Slocum glider. Two types of active roll control mechanism are designed and evaluated in this chapter. The main purpose of the active roll control mechanisms is to provide adequate control of the roll motion of the glider which is currently manoeuvred by the tail rudder.

With the mechanisms presented in this chapter, we are expecting to enhance the stability and disturbance rejection in the 3 DOF sawtooth gliding pattern, and to expand gliding patterns of the Slocum glider, such as the spiral motion and banked turn with a small radius.

The Autonomous Roll Trimming Mechanism (ARTM) is designed to simplify the ballasting process. It also poses a trend of autonomous ballasting and the possibility of on mission ballasting. The Deflectable Wing Mechanism (DWM) shows the potential of large range roll angle controllability.

3.1 Autonomous Roll Trimming Mechanism (ARTM)

3.1.1 Mechanism Overview

Initially, the glider is approximately trimmed to a zero stationary roll angle and neutral buoyancy (corrected for saltwater density of 1025kg/m^3) in the deep water tank prior to the mission. However, the trimming process is inconvenient. Even worse, a small roll angle error (5^o) always exists during the flight due to the mis-trim. (Figure 2.8 shows a small roll angle error in the field trial). Based on the former experience of the trimming process following the procedures outlined in [51], the zero static roll angle is hard to achieve and the roll ballast process is time consuming. Thus, a concept of ARTM is proposed.

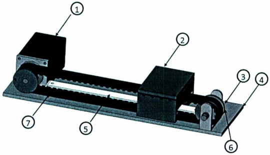

Figure 3.1: Autonomous Roll Trimming Mechanism Solidworks Assembly

Figure 3.1 shows the Solidworks assembly of ARTM. The mechanism is evolved from the trim weight defined in the mathematical model. A mass attached to a timing belt is driven by a stepper motor in the wingspan direction. Therefore, the CG of the glider becomes adjustable in the wingspan direction.

The ARTM's electrical charateristics are described below.

1. Easy Switch. The ARTM can be easily powered on/off via a relay without

disassembling the hull. The commands are transmitted through an underwater plug or wireless communication.

2. Low power consumption. After the ballasting the ARTM can be set in the sleep mode with minimum power consumption. The mass position in the ARTM is preserved which keeps the static zero roll angle of the Slocum glider.

3. On mission trimming. During the mission, some environmental disturbances, such as algae, may cause position shifting of the CG. The operator can wake up the ARTM, and execute an on-mission trimming.

Table 3.1: Part List of Autonomous Roll Trimming Mechanism

Part No.	Item	Description
1	Stepper Motor	NEMA Size 11
2	Trim Weight	Lead or brass, weight 1kg
3	Pulley Support	Support and fix the pulley shaft
4	Plate	Support the whole mechanism
5	Transition Track	The track for weight to move
6	Pulley	Small plastic pulley for timing belt
7	Timing Belt	Attached to the trim weight

3.1.2 Steady Equation and Simulation

Figure 3.2 shows a general case of the glider when the roll angle is nonzero. The trim weight is superimposed on the gravity vector shown in Figure 3.2.

By applying the conservation law of angular momentum, the steady state equation (Equation 3.1 to 3.4) of roll motion can be obtained, where p is the roll velocity, p_t is the inertia of the trim weight, and u is the input to the mechanism.

$$\dot{\phi} = p \tag{3.1}$$

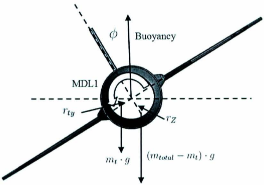

Figure 3.2: Front View of the Slocum Glider

$$J_{xx}\dot{p} = m_t \cdot g \cdot r_{ty} \cdot cos(\phi) - (m_{total} - m_t) \cdot g \cdot r_Z \cdot sin(\phi) + D_e + M_{DL1} \tag{3.2}$$

$$\dot{r}_{ty} = \frac{p_t}{m_t} \tag{3.3}$$

$$\dot{p}_t = u \tag{3.4}$$

where all the notations are displayed in Figure 3.2.

With the assumption of the small roll angle ($<10^o$), the nonlinear terms in the steady state equations can be linearized by using the approximate values that cosϕ=1, sinϕ=ϕ, $arctan(r_{mz}/r_my) = r_{mz}/r_my$, $M_{DL1} = K_{q1}pV^2$ and the steady state of V is 0.55 m/s. The disturbance is incorporated in the D_e term. Thus, the steady state equations become:

$$\dot{\phi} = p \tag{3.5}$$

$$\dot{p} = \frac{1}{J_{xx}}(m_t \cdot g \cdot r_{ty} - (m_{total} - m_t) \cdot g \cdot r_Z \cdot \phi + D_e + K_{q1}pV^2) \tag{3.6}$$

$$\dot{r}_{ty} = \frac{p_t}{m_t} \tag{3.7}$$

$$\dot{p}_t = i \tag{3.8}$$

Then, we input all the known parameters (masses and hydrodynamic coefficients mentioned in Chapter 2) into Equations 3.5 to 3.8. The steady state equations become:

$$\dot{\phi} = p \tag{3.9}$$

$$\dot{p} = 2.45r_{ty} - 1.21\phi - 0.25D_e - 1.5125p \tag{3.10}$$

$$\dot{r}_{ty} = \frac{p_t}{m_t} \tag{3.11}$$

$$\dot{p}_t = i \tag{3.12}$$

Figure 3.3 shows the Simulink flow chart created based on the steady state equation (Equation 3.9 to Equation 3.11). The above one is the original Simulink file, while the one below is the modified flow chart. The inertia input p_t is obtained by applying a PID (proportional–integral–derivative) to the roll angle difference ($\Delta\phi$) between the current and desire roll angle which is zero in our case. Based on the Equation 3.11, an integrator and a constant gain is applied on the inertia input p_t. An additional saturation block is added because the range of the lateral displacement of the trim weight (r_{ty}) is restricted by the hull diameter of the glider. After that, based on the Equation 3.10, roll angle velocity p is obtained by integrating the combination of four terms. Based on Equation 3.9, the roll angle is obtained by integrate the roll velocity. During the simulation, r_{ty}, roll velocity and roll angle are observed. To analyze the control system performance we:

1. Create a disturbance term in the glider model.

2. Apply the same disturbance to the ARTM model.

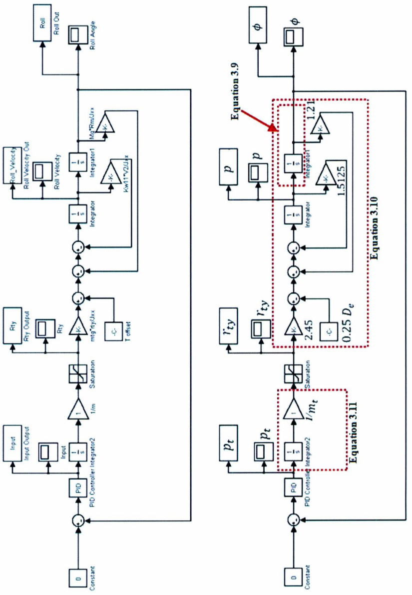

Figure 3.3: Simulink Flow Chart of ARTM

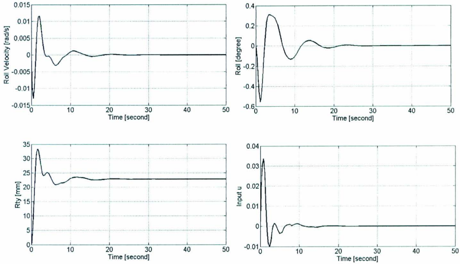

Figure 3.4: ARTM States Response in Simulink

3. Substitute the trim weight term in the glider model with the response obtained in the ARTM model.

4. Compare the performance of the glider model with disturbance before and after the ARTM is included.

The aft. battery is used for creating the disturbance. In our case, we move the aft battery 3 mm in the negative b2 direction. The disturbance (D_e) can be calculated as follows:

$$D_e = m_{bb} \cdot g \cdot r_{bby} \tag{3.13}$$

The response of the ARTM model is shown in Figure 3.4 with P_{gain}=1, I_{gain}=1, and D_{gain}=2. The mechanism settled down within 30 seconds. After the mechanism is settled the trim weight remains at a positive offsetting of 22.8 mm in the lateral

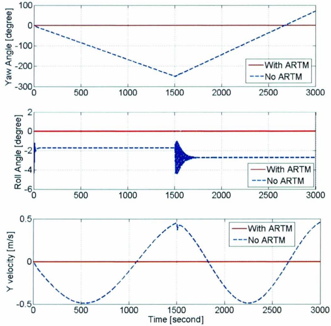

Figure 3.5: Glider Performance Comparison with and without ARTM Integrated

direction. Figure 3.5 shows the major lateral parameters comparison results of after and before the ARTM is installed. We assigned the glider change from descending to ascending at 1500 second. The high frequency oscillation appears due to the exclusion of the wing damping effect which shorten the settling time. As shown in Figure 3.5, the Slocum glider is drifting sideway with a small roll angle if the disturbance is not compensated. The drifting is eliminated with the ARTM activated. In conclusion, the ARTM shows the potential of eliminating the small roll error and simplifying the ballasting process. However, the mechanism is restricted by the space and permitted weight. In the previous examination of the 3D performance of the glider, the 3D simulation in Section 2.7 is done by offsetting the trim weight to the maximum position

(8 cm) and maximum payload capacity (1 kg). The result shows the maximum roll angle that can be achieved is 10^o which is not enough, as we expected. Although the ARTM is unable to roll the glider with a large angle, the abilities of automatic roll trimming and enhancing the straight gliding are promising.

3.2 Deflectable Wingtip Mechanism(DWM)

The ARTM introduced in the last section shows the ability of assisting the roll trimming process. However, the allowed added weight and the permissible offset in the lateral direction of the trim weight are limited inside the glider. By simulation, the Slocum glider is unable to achieve the expected roll angle ($\pm 45^o$) with the maximum operation range (maximum weight and lateral offset). As a solution, the DWM inspired from the morphing aircraft is presented in this section. The mechanism is intended to enhance the roll manoeuvre of the Slocum glider with the expectation of achieving a roll angle of 45^o in the pre-stall AOA region of the wings.

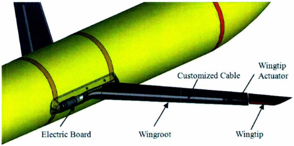

Figure 3.6: Arrangement of the Deflectable Wingtip Mechanism

In the existing AUVs, deflectable wings/rudders are integrated to improve the motion capability of the vehicle. For example, in the Arima Laboratory at Osaka Prefecture University, Professor Masakazu Arima and his colleague developed an underwater

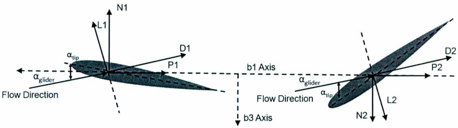

Figure 3.7: Analysis of the Forces on the Wingtips

glider with independently controllable main wings (NACA0006) ([52] and [53]). Moreover, the explorer AUV has deflectable wings as well as a deflectable X-tail rudder [23]. Beyond the underwater technology, as mentioned in section 1.3.2, the wing of the morphing aircraft is variable, corresponding to the commands. The active wings control the vehicle by varying the hydrodynamic/aerodynamic forces and torques.

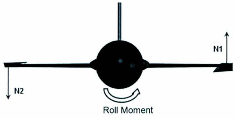

Figure 3.8: Rolling the Glider

Figure 3.6 to Figure 3.8 show the operation concept of the DWM. The original flat plate wings are replaced by wingroots and wingtips with a NACA0012 foil cross section which provides adequate space for the actuator integrated inside the wingroot. The wingtips are rotatable, which alters the hydrodynamic effect on the whole glider system. As shown in Figure 3.7, on each wing, the deflection of the wingtip creates a normal force (N) and a parallel force (P) with respect to the Body Fixed Coordinate.

In the siutation of the wingtips deflecting in the opposite direction (Figure 3.8), the normal forces on the left and right wings contribute a roll moment which rolls the glider body.

Besides activating the roll control, DWM also increases the efficiency of the glider because the foil cross section provides low drag and high lift. Furthermore, the wingtip is able to work as do the ailerons or spoilerons on the aircraft to adjust the descending/ ascending velocity of the Slocum glider.

3.2.1 Mathematical Evaluation of the Slocum Glider with Deflectable Wingtip Mechanism Integrated

Before manufacturing the mechanism, an initial estimation of the Slocum glider performance with DWM is considered. The Slocum glider is only simulated in the diving states because of the long settling time in the climbing simulation of the dynamic model. [54] and [55] comprehensively introduced and discussed the airfoil lift and drag force, based on which the wingtip hydrodynamic effect can be accurately estimated. However, for the initial estimation, we only emphasize the potential capability of the DWM. The maximum achieveable roll angle in the pre-stall region of the wingtip is estimated with the assumptions that:

1. Only the wingtip hydrodynamic forces and torques are included.
2. The simulated wingtip is straight with zero sweep angle and zero tapered angle.
3. The chord length of the wingtip is assumed to be 12 cm with a wingspan of 15 cm.
4. The distance in the b2 direction between the wingtip center and Body Fixed Coordinate origin is 0.5m.
5. Neglect the pitch moment created by wingtip.

6. Neglect the influence in the deflection transition area between the wingtip and wingroot.

The lift and drag force of wingtips can be calculated by using hydrodynamic Equations 3.14 and 3.15, then converted into the normal forces (N) and parallel force (P) in the Body Fixed Coordinate, which are expressed in Equation 3.16 to Equation 3.19.

$$L_W = \frac{1}{2}\rho A C_{LW} V^2 \tag{3.14}$$

$$D_W = \frac{1}{2}\rho A C_{DW} V^2 \tag{3.15}$$

$$N_1 = L_1 cos\alpha_{glider} + D_1 sin\alpha_{glider} \tag{3.16}$$

$$P_1 = -L_1 sin\alpha_{glider} + D_1 cos\alpha_{glider} \tag{3.17}$$

$$N_2 = L_2 cos\alpha_{glider} - D_2 sin\alpha_{glider} \tag{3.18}$$

$$P_2 = L_2 cos\alpha_{glider} + D_2 sin\alpha_{glider} \tag{3.19}$$

As mentioned, in the situation of the wingtips deflecting in the opposite direction, a roll torque is created by the deflection of wingtips and formulated in Equation 3.20, where the r_{tipy} is the lever arm of the normal forces.

$$M_{wing} = (N_2 + N_1) r_{tipy} \tag{3.20}$$

The hydrodynamic coefficients of the NACA0012 foil are obtained via an online source, Javafoil [64].The Reynolds number (Equation 3.21) of the wingtip is calculated based on the assumed wingtip dimension, where the ρ_{SW} is the density of the salt water, and μ_{SW} is the dynamic viscosity of the salt water.

$$Re = \frac{\rho_{SW} V(ChordLength)}{\mu_{SW}} \approx 60K \tag{3.21}$$

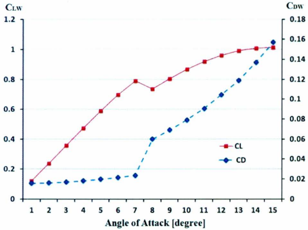

Figure 3.9: Lift and Drag Coefficient of NACA0012 Obtained in JAVAfoil, Re=60 K

Figure 3.9 shows the C_{LW} and C_{DW} plot obtained in Javafoil. We observe that a significant increase of drag coefficient and a decrease of lift coefficient exist between 7^o and 8^o of AOA, which means the wing starts stalling at 8^o of AOA. Thus, the AOA of the wingtips on two wings are set to $\pm 7^o$ which creates a maximum wingtip roll torque without stalling, in the simulation.

Figure 3.10 shows the glider performance with wingtip effects included. As we expected, the glider spiralled down with a roll angle of 45^o and radius of 7 meters. The roll torque created by the wingtips is also presented in Figure 3.10. Overall, the simulation shows the DWM is a potential roll control module which rolls the glider between $\pm 45^o$.

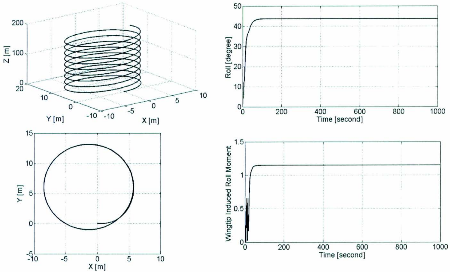

Figure 3.10: Slocum Glider Performance with Wingtip Deflected

3.2.2 Qualitative Illustration of Spiral Motion and Roll Manoeuvre Recommendation

As shown in Section 3.2.1, the DWM shows the capability of rolling the Slocum glider with a maximium roll angle of 45^o before stalling. In this section, the effect of AOA of the wingtip is qualitatively illustrated. A series of simulations were performed to examine the spiralling equilibrium performance in respect to the AOA of the wingtips. Furthermore, the control strategies of roll and lateral manoeuvres are discussed.

In the serial simulation, the AOA of the wingtips on both sides are set with the same value but in the opposite directions. The Slocum glider peroformance is simulated under various AOA of wingtips with a 1^o increment from 1^o to 15^o which includes the pre-stall and stalled region of the foil. Figure 3.11 and Figure 3.12 show the trend of spiraling parameters (roll angle, wingtip induced roll torque, turning radius, and turning rate) in respect to the AOA of the wingtips. The observation, explanation and discussion are as follows:

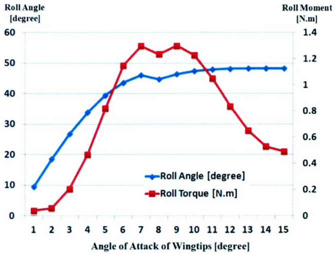

Figure 3.11: Roll Angle and Roll Moment Created by Wingtips in Spiraling Motion

1. All the spiral parameters except the turning radius have a significant decrease from 7^o to 8^o of AOA. This is caused by the decreasing of the lift coefficient in the transition between unstall to stall.
2. The roll angle and turning rate increase, and the turning radius decreases with the increases of AOA of wingtip. However, they finally converge as the wingtip AOA increases.
3. The roll torque is increasing with the increase of AOA in the pre-stall region, while it is decreasing in the stalling region, due to the drag force dramatically increasing in the stalling region, the translational velocity and the increased AOA of the glider (Figure 3.13). Based on Equation 3.16, the drag force-induced

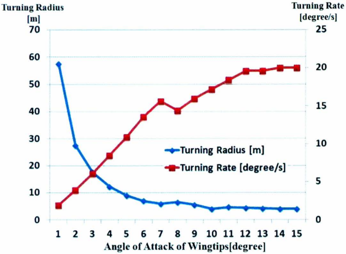

Figure 3.12: Turning Radius and Rate in Spiral Motion

normal force increased with the increasing of AOA of the glider, but lift force-induced normal force decreased in the normal force expression. The normal force increase induced by the drag force is relatively small compared to the decrease induced by the lift force. Therefore, the normal force decreased with the increasing of the wingtip AOA when stalling. As a result, the wingtip induced roll torque decreases in the stalling region.

4. Although the wingtip-induced roll torque decreased, the roll angle is still increasing. Because of the decreasing of velocity, the hydrodynamic torques M_{DL1} also decrease, which means that with a smaller roll torque the same roll angle still can be achieved.

The parametric study of the equilibrium state of the spiral motion reveals some recommendations for controlling the 6 DOF motion of the Slocum glider. This qualitative

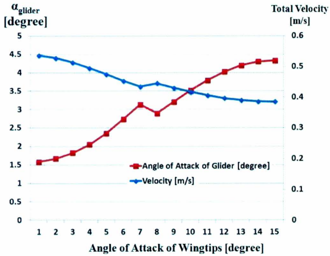

Figure 3.13: The Glider Parameters in Spiraling

investigation shows that a large control range over the roll angle and turning radius can be obtained with a small range variaton of the AOA of the wingtips.

The lateral manoeuvre of the Slocum glider is potentially improved with the DWM integrated, and the glider is able to fulfill the ice profiling as mentioned in Section 1.3. To avoid collision and to point the profiling sonar toward the iceberg, the turning radius and roll angle are critical in the spiral ice profiling mission. By parameterizing the spiral equilibrium, the roll angle can be controlled up to 48^o by turning the AOAs of wingtips. The rudder should be involved to work together with the DWM to control the spiral radius. The operator can first command the DWM to roll the glider, then use the rudder to correct the heading. The control method and design will be included in future work.

3.2.3 The Design of Deflectable Wingtip Mechanism (DWM)

After the model based evaluation, we start the manufacturing of the DWM. As shown in Figure 3.6, the standard flat-plate glider wings are replaced by carbon fiber wing-roots and wingtips in NACA0012 profile. The Wingtip Actuator Assembly is clamped inside the hollow wingroot section, while the shaft extension is fixed to the wingtip by set screw. A miniature geared stepper motor, controlled by the pcb board located inside the wing attachment, alters the deflection angle between wingroot and wingtip.

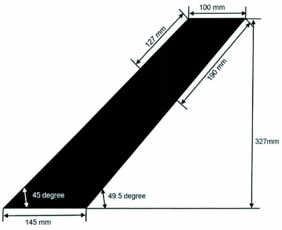

Figure 3.14: Dimension of the DWM Wing Platform

Instead of designing the straight wing which is simulated in Secion 3.2.1 and 3.2.2, the NACA0012 wing is designed with the same platform as in the original flat wing to allow performance comparison. The wing is designed with a tapered backward swept platform (Figure 3.14). The sweep angles of the leading edge and the trailing edge are 45^o and 49.5^o respectively. The chord length is 14.5 cm at the root and 10 cm at the tip, and the wingspan of wingtip and wingroot are 127 mm and 200 mm separately.

The swept angle and taper angle effects are discussed in [54] and [55]. The content in Chapter VII-8 in [55] and Chapter XV of [54] can be used to correct the experimental test data and the simulation data. The rotating axis of the wingtip is located at the maximum thickness point and parallel to the trailing edge. The electronic control board is intended to be installed inside the new attachment enclosure close to the glider hull.

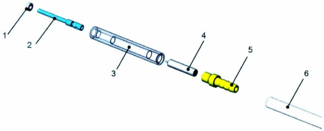

Figure 3.15: Explored View of Wingtip Actuator Assembly

Table 3.2: Part List of Wingtip Actuator Assembly

Part No.	Item	Manufacturer
1	Ceramic Bearing	BOCA Bearing Company
2	Shaft Extension	Technical Services at MUN
3	Motor Pressure Housing	Technical Services at MUN
4	Stepper Motor	Micro Motion Solution
5	Hose Barb Endcap	Technical Services at MUN
6	Tygon Tubing	McMaster Carr

The exploded view of the Wingtip Actuator Assembly is shown in Figure 3.15, and the details of the parts are listed in Table 3.2. The miniature stepper motor (6 mm in diameter with a 256:1 ratio gearhead included) is selected for rotating the wingtip and preserving the deflection angle against the hydrodynamic torque. Furthermore, the motor housing is designed for enduring the hydrodynamic pressure for up to 200m of depth. A customized cable, which includes a hose barb endcap and Tygon tubing, is used to waterproof the wires between the motor and control board. The assembly is sealed by a dynamic rotation O-ring [56] located on the shaft extension, a fitting tube o-ring [56] between the hose barb endcap and the housing, as well as with a hose clamp on the tygon tubing. The motor wires are running inside the tygon tubing, and the assembly is filled with oil. As shown in Figure 3.16 the actuator assembly has an overall length of 121.5 mm and diameter of 10 mm.

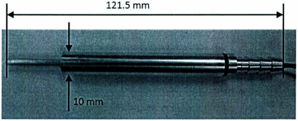

Figure 3.16: Dimension of Wingtip Actuator Assembly

The new wingroot, wingtip, and the attachment enclosure are made of carbon fiber. [57] and [58] discuss the composite material fabrication process and methods. The Vacuum-bag molding technique (Figure 3.17) is used in the wing manufacturing. The peel ply helps the epoxy evenly distribute in the fiber, while the breather is used to absorb the extra epoxy. The demolding becomes easier when the release ply is between the peel ply and the breather. Finally, the mold area is vaccumed by using a bagging film and a vacuum pump (Figure 3.18). Three layers of carbon fiber are used in the wing, a $0^o/90^o$ in the center and a $\pm 45^o$ at the top and bottom. Because of the limited space in the original wing attachment part, a new attachment which provides the space for the DWM control board is manufactured. The carbon fiber is laid on a foam mold of the attachment with the same carbon fiber schedule as the wing. After the epoxy is cured, we use the aceton to melt the foam inside. Finally, the wing and the new attachment are glued together by structure filler mixed epoxy.

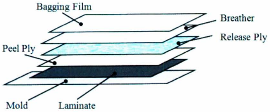

Figure 3.17: Layup of Vacuum-bag Molding Technique

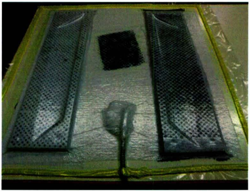

Figure 3.18: Curing

The painting layers are shown in Figure 3.19. The painting schedule is based on car painting technology. All the materials used are listed in Table 3.3. The painting steps are discussed below.

1. Dry and wet sanding with different grits (80-240) sandpaper is applied on the wing.

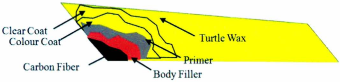

Figure 3.19: Paint Layer

Table 3.3: Painting Material List

Name	Description	Manufacturer
Body Filler	Smoothen surface and fill the void	Bond Corporation
Primer	Ensure the adhension of the paint to the surface	Dupli-Color Product Company
Colour	Premium Automotive Paint	Dupli-Color Product Company
Clear Coat	Acrylic Crystal Clear Coat	Krylon Product Group
Surface Wax	Coat protection and smoothen the surface	Turtle Wax

2. Use the body filler to fill the void on the surface, then sand the surface with various grits (80-240) sandpaper.
3. Repeat Step 2 twice.
4. Clean the surface, spray the primer, dry and wet sand the surface with a 1200 grit sandpaper after the primer dries.
5. Repeat Step 4 at least 3 times.
6. Clean the surface, spray the colour coat, dry and wet sand the surface with a 1200 grit sandpaper after the paint dries.
7. Repeat Step 6 until the surface colour is uniform.
8. Clean the surface, spray on the clear coat.

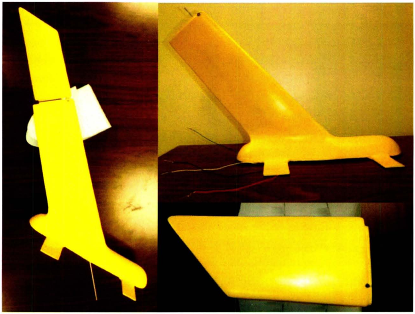

Figure 3.20: Deflectable Wing Mechanism

9. Use turtle wax to smooth the surface.

A finished set of DWM is shown in Figure 3.20. To mount the DWM on the hydrodynamic testing platform (See Section 4.2), additional rectangular flanges are attached.

3.2.4 The Control of Deflectable Wingtip Mechanism

A Baby Orangutan B-328 Robot Controller (1.2" × 0.7") [59] manufactured by Pololu Robotics and Electronics is selected to control the actuator and communicate with the Slocum glider. An ATmega 328p microcontroller [60] and a dual H-bridge (TB6612FNG [61]) are integrated onboard. The required pins, such as the Serial Peripheral Interface(SPI) pins, Universal Asynchronous Receiver/Transmitter(UART) pins, and motor control signal pins, are configured on the output port. The board is operated at 20 MHz with an input voltage range from 5v to 13.5v, and it is intended to be sealed inside a pressure vessel located in the new attachment. The connections between the board and the actuator assembly, and the board and Slocum glider are implemented with the miniature underwater connectors manufactured by Teledyne Impulse installed on the endcap at both ends.

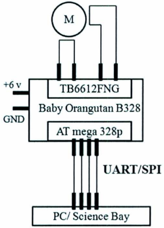

Figure 3.21: Connection Diagram

Figure 3.21 shows the wire diagram between the glider science bay, the Baby Orangutan, and the stepper motor. The SPI pins are connected to the Slocum glider science bay which has a CF1 Persistor ([62] and [63]) with Queued Serial Peripheral Interface(QSPI) communication ports. The bipolar stepper motor is driven by the signal created from the H-bridge with a full-step drive method(two phases on) under 6v. As well, the test mode is also available, in which the system is controlled by the operator via PC software, such as Matlab. The data and commands are transferred using the UART communication method.

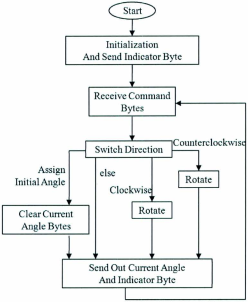

Figure 3.22: Flow Chart of the Control of DWM

The flow chart of the control of DWM is shown in Figure 3.22. The initialization includes SPI/UART communication initialization, stepper motor initialization, and clearing the current angle bytes. Once the initialization and rotation are finished, the indicator bytes which notify that the system is ready are transmitted to the terminals (Science bay/PC) to require commands in succession. A typical command from the terminals consists of 5 bytes. It starts with the acknowledge(0xFF) byte and follows with operation bytes and ending bytes(0xEE). The operation command includes the direction, speed, and steps bytes, based on which the H-bridge output is generated. In the operation states, the user is able to assign any angle as initial angle. After each rotation, the board estimates the current wingtip deflection angle with respect to the initial angle. The current deflection angle bytes are transmitted and stored in the flash on the Slocum science bay, or recorded by the PC software. In our initial operation concept, after the wingtip is install we can zero the wingtip manually by sending the rotating command to the system. Once the wingtip is aligned with the wingroot (home position), we can initialize the deflection angle, and set the current angle to zero. Alternatively, a homing sensor, such as a hull effect sensor could be installed for automatic initialization.

Chapter 4

Evaluation and Analysis of Deflectable Wingtip Mechanism (DWM)

In Chapter 3, the DWM shows the potential of rolling Socum gliders approximately 45^o. However, the accuracy of the hydrodynamic coefficient created by the Javafoil software has to be validated. Because of the environmental factors, such as surface smoothness and boundary conditions, the software generated coefficient is different from the realistic case. Consequently, the model based control strategy which is selected to control the roll angle is not able to control the roll angle of the Slocum glider if the hydrodynamic coefficient is inaccurate. In this chapter, a hydrodynamic test was applied on the DWM to investigate the actual hydrodynamic performance. With a designed testing paltform, the experiments were conducted in the open water flume tank in the Fluid Laboratory at the Faculty of Engineering and Applied Science, MUN. The discussion and comparison of the DWM hydrodynamic test result are also included in this chapter.

4.1 Hydrodynamic Testing Device Information

4.1.1 Open Water Flume Tank at MUN

The open water flume tank (32' long × 17" wide × 22" deep) (Figure 4.1) in the Fluid Laboratory is located in the Engineering Building at MUN. The flow is regulated by a butterfly valve and a depth gate at the end of the tank. In the hydrodynamic test the water velocity is operated between 38 cm/s and 50cm/s. The velocity setting is further discussed in section 4.2.2

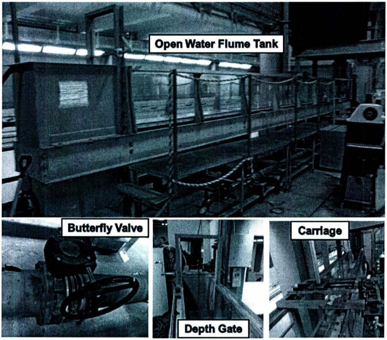

Figure 4.1: Open Water Flume Tank

4.1.2 Hydrodynamic Platform Design

Figure 4.2 shows the SolidWorks assembly of the hydrodynamic platform which is designed for mounting the DWM on the flume tank. The detailed drawings of the parts are documented in Appendix A.2. The spporting beam is made of a 90^o angle aluminum channel, which provides the strength to support the platform across the tank. The cross beams are fixed on the flume tank with C-clamps. Under the Fixed Plate, the swept angle of the DWM is variable with a hinge attached between the Top Plate and the Bottom Plate (Figure 4.2). Because of being attached to the rotation disc between the load cell and the Fixed Plate, the DWM is rotatable in the horizontal plane. Most importantly, the wingtip deflection angle can be altered via a 1/8" diameter shaft through the wingroot. On the customized platform, the hydrodynamic performance of the DWM with various AOA sweep angles, and wingtip deflection angles, can be investigated.

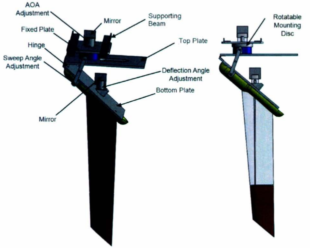

Figure 4.2: Hydrodynamic Test Platform

4.1.3 Load Cell Information

To measure the forces and torques, a multi-axis force and torque load cell (Figure 4.1) manufactured by JR3 Load Cell Company is mounted on the platform with its axes aligned with the axes of the Body Fixed Coordinate defined in Chapter 2. The specification of the load cell is listed in Table 4.1. One disadvantage of the load cell is its inaccuracy. As seen in Table 4.1, the nominal accuracy in each axis is 1%. The random error of the forces in x and y direction is 0.67 N, which is a significant amount of error compared to the lift and drag force in our scenario. Thus, we conducted at least 2 sets of experiments to minimize the random error caused by the load cell itself.

Figure 4.3: JR3 Load Cell

Table 4.1: JR3 Load Cell (67M25A-I40-DH) Capability Specification

Characteristics	F_x, F_y	F_z	M_x, M_y	M_z
Full Scale	15 lbs	30 lbs	40 in-lbs	40 in-lbs
Load Ratings	25 lbs	50 lbs	66 in-lbs	66 in-lbs
Resolution	0.006 lbs	0.01 lbs	0.02 in-lbs	0.02 in-lbs
Nominal Accuracy	1%	1%	1%	1%

1 lbs=4.445 N, 1 in-lbs=0.113 N-m

4.1.4 Laser Angle Measurement

The deflection angle measurement is implemented by using a green point laser (manufactured by Apinex Inc.) and a mirror on the structure. Figure 4.4 shows the basic concept of the measurement methodology. Firstly, the laser is rotated to our desired angle a (see Figure 4.4). Then, we flash the laser to the center of the mirror. After that, we rotate the mirror to align the reflected laser point with the laser point vertically. When they are aligned as shown in Figure 4.4, the angle b is equal to our desired angle a.

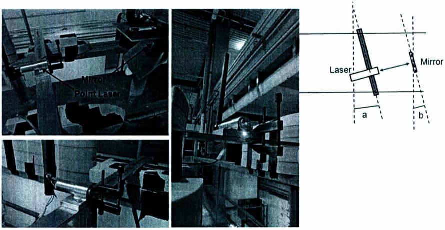

Figure 4.4: Point Laser Angle Measurement

4.1.5 Water Velocity Sensor

The water velocity is measured by the Vectrino Velocimeter (Figure 4.5), an Acoustic Doppler Velocimeter manufactured by the Nortek AS Company [66].The sample volume is located at 5 cm under the sensor probe which consists of four receiving transducers. The transmit transducer is in the center of the probe. The velocity sensor has a sampling frequency of up to 25 Hz and measurement range of up to 4 m/s with an accuracy of 1 mm/s. The sensor interfaces with computers via a serial port, and the velocity measurement can be collected and plotted in the vendor software, Vectrino. During the experiment, the sensor is mounted on the carriage on the flume tank and located upstream of the platform. It measured the water flow velocity at the center of the submerged wing and align with the assembly at the center of the tank width, the depth of the velocimeter varied depending on the wing orientation (See Table 4.3).

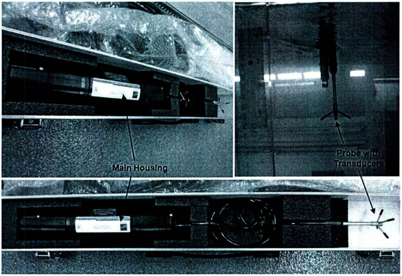

Figure 4.5: Water Velocity Sensor

4.2 Testing Strategy

4.2.1 Experiment Planning

The experiments are applied on the vertical and the swept wing orientations. The vertical configuration is an alternative option for future modification, while the swept configuration shows the current design concept and matches the current wing design of Slocum gliders.

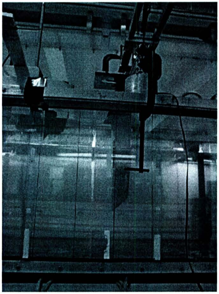

Figure 4.6: Vertical Wing Orientation Setup

The DWM in Figure 4.6 is oriented in the vertical setup, in which the deflection occurs parallel to the incoming water flow. It minimizes the complicated water flow pattern happening around the deflection area. However, the angle of the tip end will create an upward force to the system which may cause the lift and drag to be different from a bottom flushed tip profile. The wingtip deflection angle varies from -20^o to $+20^o$.

The DWM in Figure 4.7 is oriented in the swept configuration and investigated with a wingtip deflection angle ranging from -20^o to $+20^o$. The experiment helps us analyze the performance of the wingtip deflection with the current design. With the same wing orientation, we covered the deflection area with ducktape, and collected the experiment data with different AOA, ranging from -20^o to $+20^o$ of the whole wing. By doing this the overall performance of the NACA0012 swept back wing is investigated.

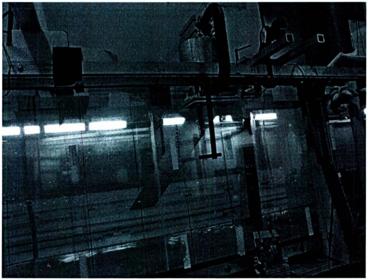

Figure 4.7: Swept Wing Orientation Setup

Each series of experiments includes a prior cross-talk calibration and the main in tank testing. The cross-talk calibration is introduced in section 4.2.3. It helps us investigate the axial cross talk effect by applying a known force in each direction. On the other hand, a series of experiments with various angle factors, such as the wingtip deflection angle and the overall AOA, are conducted in the main testing. In the vertical configuration and the first stage of the swept configuration, the wingroot stays at a zero AOA, while the wingtip deflects from -20^o to $+20^o$ with an increment of 2.5^o. At each individual angle, 4 sets of load data are recorded at 50 Hz. Firstly, a 20 second data series is collected before the water flows in. Then, the second set of data (Transition Data) illustrates the load variation on the structure from the dry condition to the steady state condition in the water. The third set (Test Data) is collected after the water settles. Finally, another set of data is recorded after the assembly is above the water and after the tank is off. It is used to compare the load change before and after the experiment. Figure 4.8 shows an example of a raw measurements of F_y. The pre dry data, test data and the Aft Dry data are same length, while the transition data are longer than the others. The steady state value of output of the load cell while DWM is in water and in dry is obtained by averaging the sample of dry load and the testing load.

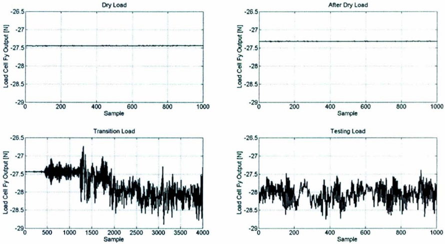

Figure 4.8: An Example of Recorded Data in Fy Direction

4.2.2 Experiment Log

The experiments lasted 3 weeks in 2012, from Feburary 5th to March 1st. In the experiments with vertical wing configuration, the water velocity was operated at 40 cm/s, 45 cm/s, and 49 cm/s separately, while the water velocity in the experiments with swept wing configuration was fixed at 49 cm/s. The investigated wingtip deflection angle ranged from -20^o to $+20^o$. Table 4.2 shows the setup of each set of the experiments, and Table 4.3 shows the tank setup for different wing configurations.

Table 4.2: Experiment Log

No.	Date	Water Velocity	Wing Configuration	Rotation Angle
1	Feb.7th	45 cm/s	Vertical	Wingtip Deflection Angle
2	Feb.8th	45 cm/s	Vertical	Wingtip Deflection Angle
3	Feb.10th	45 cm/s	Vertical	Wingtip Deflection Angle
4		49 cm/s	Vertical	Wingtip Deflection Angle
5	Feb.13th	49 cm/s	Vertical	Wingtip Deflection Angle
6	Feb.15th	40 cm/s	Vertical	Wingtip Deflection Angle
7	Feb.17th	40 cm/s	Vertical	Wingtip Deflection Angle
8	Feb.21st	49 cm/s	Swept	Wingtip Deflection Angle
9	Feb.23rd	49 cm/s	Swept	Wingtip Deflection Angle
10	Feb.28th	49 cm/s	Swept	AOA of the Glider
11	Feb.29th	49 cm/s	Swept	AOA of the Glider

4.2.3 Cross-Talk Calibration

Although the JR3 load cell is self-calibrated to eliminate the decoupling effect, the cross-talk still exists due to the mechanical properties of the mounting structures, the screws, and the offsetting of the load cell from the acting point of the forces. For example, the drag force, which acts on the submerged wing section, will create a torque in the Y direction (Figure 4.9), which in advance influences the force in Y direction. However, we found that the cross-talk effect of applied torque is negligable

Table 4.3: Experiment Setup with Different DWM Orientations

Parameters	Vertical Configuration	Swept Configuration
Water Depth	43 cm	36 cm
Wing Bottom to Tank Bottom Distance	16 cm	15 cm
Wing Vertical Submerged Length	27 cm	21 cm
Velocity Transducer Position to the Bottom	30 cm	25 cm
Submerged Wing Platform Area	193.8923 cm^2	231.8738 cm^2

compared to the cross-talk induced by the force. Therefore, the cross-talk calibration is only applied on the axes of forces (F_x, F_y, and F_z).

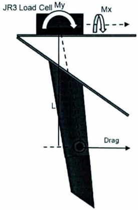

Figure 4.9: Cross-Talk Effect

The cross-talk calibration process was carried out before each series of tank tests. The purpose of the calibration is to obtain the intersectional influence by applying known weights on each direction. Then, by inversing the relationship between the weight and output measurement, we can calculate the actual force based on the collected output.

(See [67] for detail).

Figure 4.10 shows the cross-talk calibration in the F_x direction. A weight of 127 grams (right) and 255 grams (left) were hung vertically and attached on a wire via a pulley, to the other end which was tied to the wing.

The cross-talk calibration was applied on the F_x, F_y with ±127g and ±255g. In the F_z, a 127g and 255g weight were applied in the positive direction, while a bucket test was applied to monitor the cross-talk effect of the upward force in the F_z direction. In the bucket test, we submerged the assembly into still water. The submerged area was the same as in the testing.

Figure 4.10: Cross-Talk Calibration on Fx Direction

Equation 4.1 shows the relationship between the output (Q) of the load cell and the actual forces (F), in which Q is a 3×n matrix including the output of 3 directions (F_x, F_y, and F_z) corresponding to the actual force F in the calibration n.

$$Q_{3\times n} = M_{3\times 3}F_{3\times n} \tag{4.1}$$

The $M_{3\times3}$ can be obtained by using the Moore Penrose Pseudo Inverse Method as shown below.

$$QF^T = MFF^T \tag{4.2}$$

$$QF^T(FF^T)^{-1} = M \tag{4.3}$$

4.3 DWM Flume Tank Test and Result

4.3.1 Experiment Process

Figure 4.11 shows an overview of the experiment setup. The load cell output is collected by a desktop computer with an executable program created using the C^{++} language. The water velocity is observed using Vectrino software interfacing with the velocimeter.

Eleven sets of experiments with 5 different experimental conditions were conducted in 3 weeks. After a series of experiments, we applied the cross-talk calibration matrix to the recorded output to obtain the actual forces. Equation 4.4 to Equation 4.7 were applied to calculate the lift coefficient (C_L) and drag coefficient (C_D), where A is the reference area, V is the flow velocity, F_x and F_y are the calibrated forces in x and y direction, and α is the AOA of DWM.

$$Q = Q_{Test} - Q_{Dry} \tag{4.4}$$

$$F = M^{-1}Q \tag{4.5}$$

$$C_D = \frac{cos\alpha F_x + sin\alpha F_y}{1/2\rho AV^2} \tag{4.6}$$

$$C_L = \frac{sin\alpha F_x + cos\alpha F_y}{1/2\rho AV^2} \tag{4.7}$$

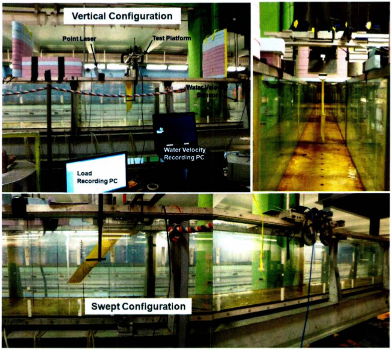

Figure 4.11: Overview of the Testing Device

To estimate the error of the experiment we took the standard deviation (σ) of the raw data at each test point. The standard deviation is plotted along the coefficient in the results. The standard deviation of the coefficient is obtained by using Equation 4.8 to Equation 4.9, where σ_F, σ_Q and σ_C are the standard deviations of the forces, load cell output, and hydrodynamic coefficients respectively.

$$\sigma_{F3\times n} = M_{3\times 3} \cdot \sigma_{Q3\times n} \tag{4.8}$$

$$\sigma_{C3\times n} = \frac{2\sigma_{F3\times n}}{\rho A V^2} \tag{4.9}$$

4.3.2 Experiment Result

Figures 4.14 to 4.18 show the C_D and C_L obtained from all the conducted experiments. The figures show the hydrodynamic performance with different wing configurations. In the experiments, the vertical tapered wing and swept-back tapered wing were examined. The Javafoil coefficients are the 2D drag and lift coefficients. However, based on the discussion of the sweep angle effect on the wings in [54] and [55], we calibrated the software created lift and drag coefficient by using Equation 4.11, where Λ is the sweep angle of the wing.

$$C'_D = C_D \cdot cos(\Lambda) \tag{4.10}$$

$$C'_L = C_L \cdot cos(\Lambda) \tag{4.11}$$

The Javafoil created coefficients are plotted with the data of experiment with the same Reynolds number. The analysis of the results is explained as follows:

1. The experiments' results with vertical configurations match the Javafoil-created coefficient well. The lift coefficient converged around the 15 degree of deflect angle. The software created data stayed inside the experiment data.

2. The tapered ratio has little influence on the hydrodynamic performance. However, in Figure 4.14 to Figure 4.16, most of the coefficient data points are smaller than the software created values.

3. The swept angle has a significant influence on the hydrodynamic performance of a wing. From our experiment result (Figure 4.17 and Figure 4.18), the coefficient does match the curve of the regular straight wing. The swept angle will be further examined.

Besides the effects of the wing configuration, other environmental factors also influ-

Figure 4.12: A Close View Inside the Tank When Angle of Attack Equals 15^o

enced the experiment results.

1. Tank Wall Effects. Figure 4.18 shows the C_L and C_D coefficient with an alternative AOA of the DWM assembly. The lift coefficient keeps increasing when the AOA is larger than 15^o. This may be caused by the wall of the tank. When the assembly is tilted, the larger the AOA of the assembly, the closer the assembly is to the wall (Figure 4.12) where the dynamic pressure of the fluid increases. Therefore, the lift and drag coefficient increases with the AOA instead of decreasing when the AOA is larger than 15^o.

2. Bent Wingtip. From the figures, especially Figure 4.18, it is seen that the hydrodynamic force is larger when the wing tilt is negative rather than positive. The reason, shown in Figure 4.13, is that the wingtip is bent towards the negative direction.

3. Load Cell Error and Negative Drag Coefficients. Based on the result of the cross-talk calibration, an upward force (buoyancy) on the DWM will decrease

the load cell output in F_x and F_y direction. Due to the accuracy of the load cell, the cross-talk calibration may not be precise enough to calibrate the output into the actual force. Thus, a result of negative drag force appears.

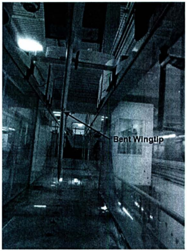

Figure 4.13: The Bent Wingtip

Consequently, we compared the hydrodynamic performance of vertical configuration DWM under different flow speeds (Figure 4.19, Figure 4.20). We found that all the curves have the same trend.

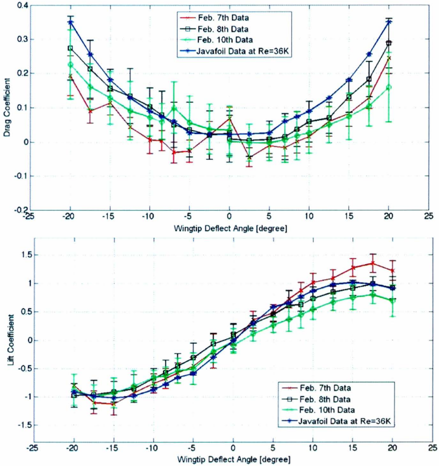

Figure 4.14: Drag and Lift Coefficient Obtained on Feb. 7th, Feb. 8th and Feb. 10th. The DWM in the Experiments are in Vertical Configuration and Flow Velocity is 45 cm/s, and the Reynolds Number is Around 36K

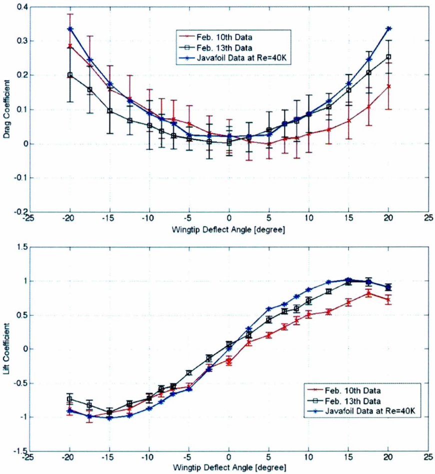

Figure 4.15: Drag and Lift Coefficient Obtained on Feb. 10th and Feb. 13th. The DWM in the Experiment are in Vertical Configuration and Flow Velocity is 49 cm/s, and the Reynolds Number is Around 40K

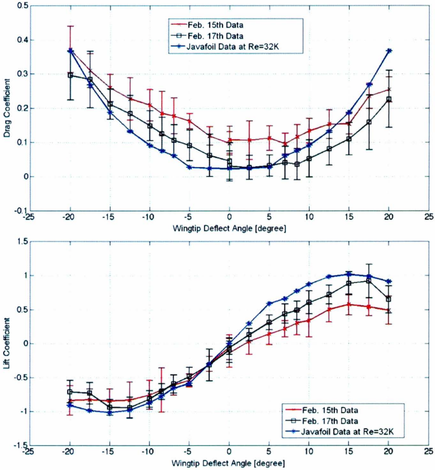

Figure 4.16: Drag and Lift Coefficient Obtained on Feb. 15th and Feb. 17th. The DWM in the Experiment are in Vertical Configuration and Flow Velocity is 40 cm/s, and the Reynolds Number is Around 32K

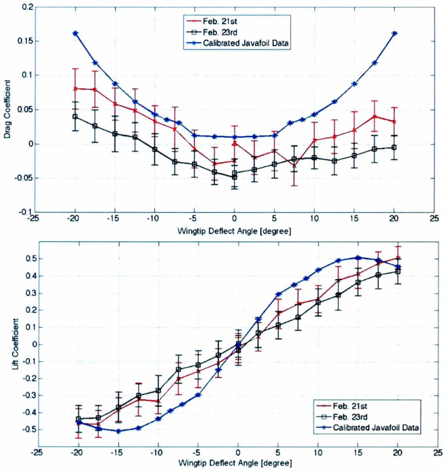

Figure 4.17: Drag and Lift Coefficient Obtained on Feb. 21st and Feb. 23rd. The DWM in the Experiment are in Swept Configuration and Flow Velocity is 49 cm/s, and the Reynolds Number is Around 58K

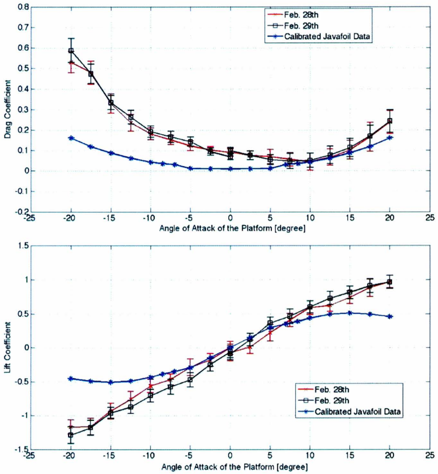

Figure 4.18: Drag and Lift Coefficient Obtained on Feb. 28th and Feb. 29th. The DWM in the Experiment are in Swept Configuration and Flow Velocity is 49 cm/s and the Reynolds Number is Around 58K

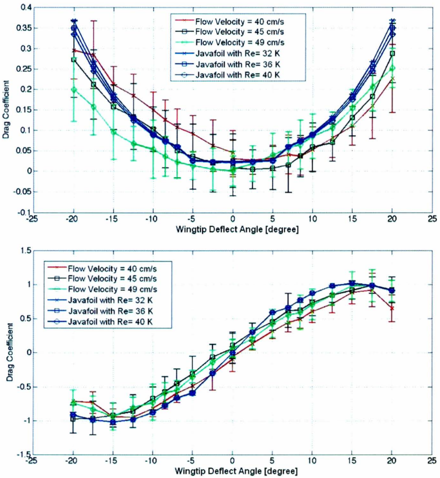

Figure 4.19: Drag Coefficient and Lift Coefficient of Vertical Configuration with Different Flow Speed

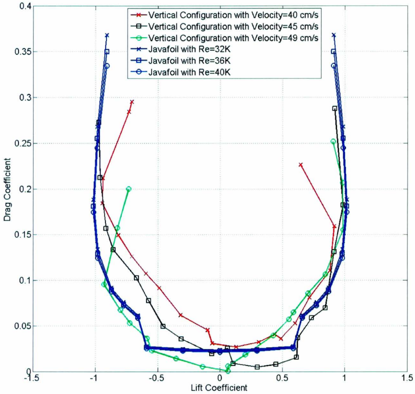

Figure 4.20: Drag Coefficient vs. Lift Coefficient of Vertical Configuration with Different Flow Speed

Chapter 5

Conclusion and Future Works

5.1 Conclusion

The main focus of this thesis is on improving the roll manoeuvrability of the Slocum glider. By expanding the roll controllability, the Slocum glider can be controlled in 6 DOF and accomplish complicated gliding patterns such as the banked turn and spiralling. With the improved roll controllability, the Slocum glider has the potential to be involved in ice management in the Newfoundland offshore industry.

In the beginning, a simplified and generalized Slocum glider dynamic model is derived based on Newton's second law. It can be modified corresponding to various internal mass distributions of the Slocum glider, or other AUVs. To evaluate the accuracy, the simulation result is compared with the field trial data collected at CBS, NL. Then the dynamic model is expanded into 3D. With the established model we can estimate the effect of the modification on the Slocum glider.

Two roll control mechanisms are introduced and evaluated in Chapter 3. The ARTM shows the ability of eliminating the roll angle error. It is a low power consumption system which simplifies the time consuming trimming process and compensates for the disturbance in the roll direction on mission. The comparison of the Slocum glider's performance with and without ARTM shows the Slocum glider maintaining a zero roll angle with ARTM instead of drifting to the side when ARTM is not activated. However, because of the limitation of the allowed additional mass and the travelling distance inside the glider hull, the ARTM is unable to roll the glider with a large roll angle. On the other hand, the DWM shows the capability of rolling the glider between $\pm 45^o$ with a relatively small wingtip deflection. The mathematical evaluation of the DWM is presented in Chapter 3. We investigated the maximum achievable roll angle with the wingtip (15cm $\times$ 12 cm with NACA0012 cross section). The result shows that a 7^o angle of attack on the wingtips on both ends rolls the glider with a 45^o angle. Furthermore, the wingtip effects are examined qualitatively. The result and discussion provide information on control strategies, such as how to obtain the desired roll angle and turning radius. After the mathematical evaluation, a DWM prototype was made, and the manufacturing process was also introduced.

Finally, the DWM performance was investigated in a hydrodynamic test. In Chapter 4, a new hydrodynamic test platform was presented. The devices, including the load cell, laser angle measurement, and the water velocity sensor, were described. The hydrodynamic testing was conducted in the open water flume tank in the Engineering Building at MUN. The drag and lift coefficients of the DWM with different wing orientations, wingtip deflection angles, and velocities were investigated and discussed. The recommendations for future experiments were also concluded.

5.2 Experiment Recommendations and Improvements

Based on the conducted experiments, we have several recommendations for improving our experiment to obtain better results.

1. A better flume tank is needed for further testing. Firstly, in the experiments conducted on Feb. 28th and Feb. 29th (rotate the whole assembly), the wing assembly was close to the wall of the tank as AOA increased, which created an error in our result. Due to the effect of water viscosity and boundary layers (wall of the tank), the water pressure is decrease with the increases of distance to the wall. The water velocity near the tank wall is lower than the center of the tank. The flow caused error will be further investigated. In addition, a large flume tank will increase the testing domain, providing a more realistic and accurate result. Finally, the experiments were conducted in the open water flume tank, where the free surface effect exists which influences the result.

2. Different platforms should be designed for vertical and swept wings. In the experiments with swept wing, the wingtip deflection axis was aligned with the swept direction instead of vertically. The deflection angle is hard to measure by using the point laser measurement. Moreover, the cross-talk effect is significantly different because the relative position of the load cell to the hydrodynamic force changes. Furthermore, the center lines of the structure in each direction have to be marked out, which is helpful in weight aligning in the cross-talk calibration, platform mounting and the zero AOA setup.

3. A high-accuracy load cell needs to be selected. Based on the load cell output in the conducted experiment, the full-scale forces rating in X and Y directions has to be at least 60 N, and force rating in the Z direction depends on the weight

of the platform. Since accuracy is significant to the result, the error of the load cell itself should be negligible compared to the drag and lift force.

4. Although a steady flow can be generated in the employed flume tank, the velocity is still oscillating within a range of 4 cm/s. In the data recording aspect, a time axis needs to be added. This would help us to synchronize the force data and the water velocity data. Thus, the error of the inconstant water velocity can be filtered.

5. In future experiments, wings with different orientations or swept angles will be made by Rapid Prototype machine. The wingtip and wingroot will become solid. Therefore their buoyancy will be easy to calculate.

6. We should increase the flow velocity difference, and expand the testing range of the Reynolds number. By increasing the difference, the performance of the DWM will be analyzed under different flow types, such as laminar flow and turbulent flow.

7. Flow phenomena. In our conducted experiment, we did not include the discussion about the vortex influence. The flow speed is setup in the range of glider flying speed. The main purpose of the experiment is to estimate the overall hydrodynamic effect of the wing assembly at glider operating condition. However, in the future, the vortex and flow type will be investigated and discussed, for example the hoseshed vortices around the foil and the flow pattern at the deflection area.

5.3 Future Works

In the first place, we will verify our collected experiment data. We will look into the raw data, and try to find the source which caused the offset of the drag coefficient of the experiment with vertical configuration and water velocity at 40 cm/s.

Then, we will improve the experiment process. In the current experiment, the factors, including the vibration of the tank structure, load cell error, the cross-talk calibration error, water velocity variation, and free surface effect influence our result. The DWM will be installed on the Slocum glider and tested in the flume tank at the Marine Institute, MUN, with an actuator assembly installed. The modified Slocum glider will be fully submerged with a load cell inside the vehicle. This experiment setup will help us eliminate most of the influence factors.

For the future development of the DWM, the factors that affect the DWM performance-such as the sweep angle, tapered ratio, deflection transition, and cross section profile-will be investigated using the Design of Experiment Method. Various solid wing models will be fabricated by the Rapid Prototype Machine available in the Engineering Department, MUN. Meanwhile, a series of CFD simulations will be done to compare to the experimental results.

For the electrical aspect, the control system will be upgraded. Instead of the stepper motor which now rotates the wingtip, a servo motor with encoder will be used. The encoder will provide us with an accurate deflection angle data and angle controllability.

Bibliography

[1] M.Moline, P. Bisset, S. Blackwell, J. Mueller, J. Sevadjian, C. Trees, and R. Zaneveld, *An Autonomous Vehicle Approach for Quantifying Bioluminescence in Port and Harbors*, Proceeding of The International Society for Optical Engineering, Vol. 5780, March, 2005.

[2] A.L. Forrest, H. Bohm, B. Laval, E. Magnusson, R. Yeo, and M. J. Doble, *Investigation of Under-ice Thermal Structure: Small AUV Deployment in Pavilion Lake, BC, Canada*, Oceans' MTS, 2007.

[3] K. Nagahashi, T. Ura, A. Asada, T. Obara, T. Sakamaki, K. Kim, and K. Okamura, *Underwater Volcano Observation by Autonomous Underwater Vehicle "r2D4"*, Oceans- Europe, 2005.

[4] Henry Stommel, *The Slocum Mission*, Oceanography, April,1989

[5] S. Jenkins, D. Humphreys, J. Sherman, J. Osse, C. Jones, N. Leonard, J. Graver, R. Bachmayer, T. Clem, P. Carroll, P. Davis, J. Berry, P. Worley, and J. Wasyl, *Underwater Glider System Study*, Scripps Institution of Oceanography Technical Report No. 53, May, 2003.

[6] V. Asper, G. Lee, J. Gobat, W. Smith, K. Heywood, B. Queste, and M. Dinniman,*Using Glider to Study a Phytoplankton Bloom in the Ross Sea, Antarctica*, Oceans' MTS/ IEEE, September, 2011

[7] P. Simonetti, *Slocum Glider: Design and 1991 Field Trials*, Woods Hole Oceanographic Institution, September, 1992.

[8] Autonomous Undersea Vehicle Application Center, http://auvac.org, March 11th, 2012.

[9] D. L. Rudnick, R. E. Davis, C. C. Eriksen, D. M. Fratantoni, M. J. Perry, *Underwater Gliders for Ocean Research*, Marine Technology Society Journal, Vol. 38 No. 1, Spring 2004.

[10] Canadian Seabed Research Ltd.,*Technique for Determining the Maximum Draft of an Iceberg*,PERD/CHC Report 20-46, March, 2000.

[11] R. Bachmayer, B. Young, and D.M. Holland, *Working Towards Ice Profiling Using Underwater Gliders: Operational Experience in Western Greenland*, Symposium on Unmanned Untethered Submersible Technology (UUST 07), August, 2007

[12] C. Bishop, B. Young, and R. Bachmayer, *Autonomous Underwater Glider Research at Memorial University*, Underwater Intervention, Vol. 4, No. 1, 2009

[13] C. Jones, D. Webb, S. Glenn, O. Schofield, J. Kerfoot, J. Kohut, H. Roarty, D. Aragon, C. Haldeman, T. Haskin, and A. Kahl, *Slocum Glider Extending the Endurance*, Teledyne Webb Research, UUST09, August, 2009.

[14] *Report of the International Ice Patrol in the North Atlantic* No. 95, 2009.

[15] AMEC Earth and Environmental and C-CORE, *Greenland Iceberg Management: Implications for Grand Banks Management Systems*, PERD/CHC Report 20-65, March, 2002.

[16] AMEC Earth and Environmental, R. F. McKenna and Associates, and PETRA International Ltd.,*Grand Banks Iceberg Management*, PERD/CHC Report 20-84, May, 2007.

[17] C-CORE and B. Wright and Associates Ltd., *An Assessment of Current Iceberg Management Capabilities*, PERD/CHC Report 20-33, November, 1998.

[18] J. Rossiter, *Remote sensing ice detection capabilities - East coast, Environmental Studies Research Funds*, April 1995

[19] S. J. Prinsenberg, I. K. Peterson, J. S. Holladay and L. Lalumiere, *Labrador Shelf Pack Ice and Iceberg Survey, March 2009*, Canadian Technical Report of Hydrography and Ocean Science 269, 2011.

[20] Oceans Ltd.,*Determination of Iceberg Draft and Shape*, PERD/CHC Report 20-75, June, 2004.

[21] M. Zhou, and R. Bachmayer,*Towards the Development of an Autonomous Iceberg Draft Measurement Probe*, NECEC, November, 2010.

[22] G. Hewitt, *Design of Pitch and Roll Control for IOT Glider*, National Research Council Canada, Institute for Ocean Technology Report, December 2005.

[23] M. T. Issac, S. Adams, M. He, N. Bose, C. D. Williams, R. Bachmayer, and T. Crees, *Manoeuvring Trials with the MUN Explorers AUV: Data Analysis and Observations*, Oceans' MTS, 2007

[24] J. J. Henry, *Roll Control for UAVs By Use of a Variable Span Morphing Wing*, Unversity of Maryland, 2005.

[25] H. F. Parker, *The Parker Variable Camber Wing*, Report No.77 Fifth Annual Report, National Advisory Committee for Aeronautics, Washington D.C, 1920.

[26] M. Abdulrahim and R. Lind, *Modeling and Control of Micro Air Vehicles with Biologically- Inspired Morphing*, American Control Conference, Minneapolis, Minnesota, USA, June, 2006.

[27] M. Abdulrahim, H. Garcia, G. F. Ivey, and R. Lind, *Flight Testing a Micro Air Vehicle Using Morphing for Aeroservoelastic Control*, 45th AIAA/ASME/ASCE/AHS/ASC Structures, Structural Dynamics and Material Conference, April, 2004.

[28] J. G. Graver, *Underwater Gliders: Dynamics, Control and Design*, Dissertation of Department of Mechanical AND Aerospace Engineering, Princeton University, May, 2005.

[29] B. Etkin, *Dynamics of Atmospheric Flight*, John Wiley and Sons, 1972.

[30] D. McRuer, I. Ashkenas, and D. Graham, *Aircraft Dynamics and Automatic Control*, Princeton University Press, 1973.

[31] B. W. McCormick, *Aerodynamics, Aeronautics, and Flight Mechanics*, John Wiley and Sons, 1995.

[32] T. I. Fossen, *Guidance and Control of Ocean Vehicles*, John Wiley and Sons, December, 1995.

[33] T. I. Fossen, *Nonlinear Modelling and Control of Underwater Vehicles*, Phd Thesis, Norwegian Institute of Technology, June, 1991.

[34] N. Mahmoudian, *Efficient Motion Planning and Control for Underwater Gliders*, Dissertation of Virginia Polytechnic Institute and State University, September, 2009.

[35] P. Bhatta, *Nonlinear Stability and Control of Gliding Vehicles*, Department of Mechanical and Aerospace Engineering, Princeton University, September, 2006.

[36] N. Mahmoudian, J. Geisbert, and C. Woolsey, *Approximate Analytical Turning Conditions for Underwater Gliders: Implications for Motion Control and Path Planning*, IEEE Journal of Oceanic Engineering, Vol. 35, No.1 January, 2010.

[37] J. Graver, J. Liu, C. Woolsey, N. E. Leonard, *Design and Analysis of an Underwater Vehicle for Controlled Gliding*, Proceedings of the 1998 Conference on Information Sciences and Systems, Princeton, NJ, March 1998.

[38] N. Mahmoudian, J. Geisbert, and C. Woolsey, *Dynamics and Control of Underwater Gliders I: Steady Motions*, Virginia Center for Autonomous Systems, Virginia Polytechnic Institute and State University, June, 2009.

[39] N. Mahmoudian and C. Woolsey, *Dynamics and Control of Underwater Gliders II: Motion Planning and Control*, Virginia Center for Autonomous Systems, Virginia Polytechnic Institute and State University, November 11, 2010.

[40] N. E. Leonard and J. G. Graver, *Model-Based Feedback Control of Autonomous Underwater Gliders*, IEEE Journal of Oceanic Engineering, Vol. 26, No. 4, October, 2001.

[41] B. L. Stevens and F. L. Lewis, *Aircraft Control and Simulation*, John Wiley and Sons, 1992.

[42] D. Baraff, *An Introduction to Physically Based Modeling: Rigid Body Simulation I- Unconstrained Rigid Body Dynamics*, Robotics Institute Carnegie Mellon University, 1997.

[43] S. Rotenberg, Rigid Body Dynamics,Winter, 2005, Lecture notes of CSE169 Computer Animation, University of California, San Diego, Winter, 2005.

[44] J. Roskam, *Flight Dynamics of Rigid and Elastic Airplanes*, Roskam Aviation and Engineering Corporation, Lawrence, KS.,1973.

[45] S. Berman, *Comparison of the lift, drag and pitch moment coefficients of a Slocum glider wind tunnel model with computational results by vehicle control technologies, Inc.*, Princeton University MAE 222 Course Project Report, 2003.

[46] J. G. Graver, R. Bachmayer, N. E. Leonard, and D. M. Fratantoni, *Underwater Glider Model Parameter Identification*, Proc. 13th Int. Symp. on Unmanned Untethered Submersible Technology (UUST), August 2003

[47] H. Lamb, *Hydrodynamics*, New York, NY Dover, 6th ed., 1932.

[48] I. A. Kibel, N. E. Kochen, and N. V. Roze, *Theoretical Hydromechanics*, New York, NY Wiley, 1964.

[49] J. G. Graver, R. Bachmayer, N. E. Leonard, *Underwater Glider Model Parameter Identification*, Proc. 13th Int. Symp. on Unmanned Untethered Submersible Technology, August, 2003.

[50] J. S. Geisbert, *Hydrodynamic Modeling for Autonomous Underwater Vehicles Using Computational and Semi-Empirical Methods*, Master of Science Thesis, Virginia Polytechnic Institute and State University.

[51] Webb Research Corporation, *Slocum Battery Glider Operation Manual*, Webb Research Corporation, June, 2004

[52] N. Ichihashi, T. Ikebuchi and M. Arima, *Development of an Underwater Glider with Independently Controllable Main Wings*, Proceeding of Eighteenth Interna-

tional Offshore and Polar Engineering Conference, Vancouver, BC, Canada, July, 2008.

[53] M. Arima, N. Ichihashi and Y. Miwa, *Modelling and Motion Simulation of an Underwater Glider with Independently Controllable Main Wings*, Oceans' Bremen, May, 2009

[54] S. F. Hoerner and H. V. Borst, *Fluid Dynamic Lift Practical Information on Aerodynamic and Hydrodynamic Lift*, Liselotte A. Hoerner, 1985

[55] S. F. Hoerner *Fluid Dynamic Drag Theoretical, Experimental and Statistical Information*, Mrs. Liselotte A. Hoerner, 1965

[56] Parker Hannifin Corporation, /emphParker O-Ring Handbook, Parker Hannifin Corporation, 2007.

[57] J. Wanberg, *Composite Materials Fabrication Handbook 1*, Wolfgang Publication Inc. 2009

[58] J. Wanberg, *Composite Materials Fabrication Handbook 2*, Wolfgang Publication Inc. 2010

[59] Pololu Corporation, *Pololu Baby Orangutan B User's Guide*, Pololu Corporation, 2010.

[60] Atmel Corporation, *ATMega 48A/48PA/88A/88PA/168A/168PA/328/328P Datasheet*, Atmel Corporation, 2010.

[61] TOSHIBA Corporation, *TB6612FNG Datasheet*, TOSHIBA, May, 2008.

[62] Persistor Instruments Inc., *Persistor CF1 Getting Started Guide, Rev 8*, Persistor Instruments Inc., 2000.

[63] Persistor Instrument Inc. *Persistor CF1 User's Manual*, http://www.persistor.com/doc/CF1/Docs/html/PersistorCF1UsersManual/index.htm, March, 20th 2012.

[64] Martin Hepperle, *Java Foil*, http://www.mh-aerotools.de/airfoils/javafoil.htm

[65] B. Claus, *Hybrid Glider Propulsion Module Implementation and Characterization*, Unmanned Untethered Submersible Technology, 2009.

[66] NORTEK AS Company, *Vectrino Velocimeter User Guide*, October, 2004.

[67] D. Schrand, *Cross-Talk Compensation Using Matrix Method*, Sensor and Transducers Journal, Vol. 79, Issue 5, May 2007.

Appendix

A.1 Hydrodynamic Platform Design Drawings

The drawings of all the parts of the hydrodynamic platform are included in this appendix. The parts are made by the Technic and Service at MUN.

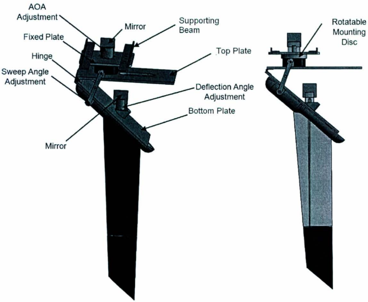

Figure 5.1: Hydrodynamic Testing Platform Assembly

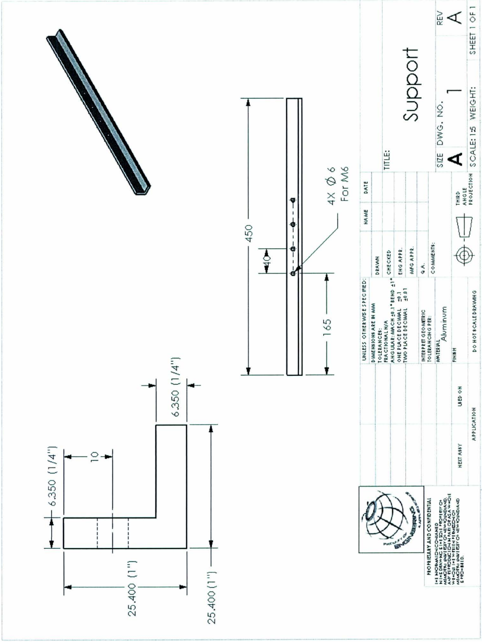

6.350 (1/4")
10
6.350 (1/4")
25.400 (1")
25.400 (1")
450
40
165
4X Ø 6
For M6
UNLESS OTHERWISE SPECIFIED:
DIMENSIONS ARE IN MM
TOLERANCES:
FRACTIONAL N/A
ANGULAR: MACH ±0.1° BEND ±1°
ONE PLACE DECIMAL ±0.1
TWO PLACE DECIMAL ±0.01
INTERPRET GEOMETRIC TOLERANCING PER:
MATERIAL
Aluminum
FINISH
DO NOT SCALE DRAWING
NEXT ASSY
USED ON
APPLICATION
DRAWN
CHECKED
ENG APPR.
MFG APPR.
Q.A.
COMMENTS:
NAME
DATE
THIRD ANGLE PROJECTION
TITLE:
Support
SIZE
A
DWG. NO.
1
REV
A
SCALE: 1:5
WEIGHT:
SHEET 1 OF 1
PROPRIETARY AND CONFIDENTIAL
1
2
3
4
5

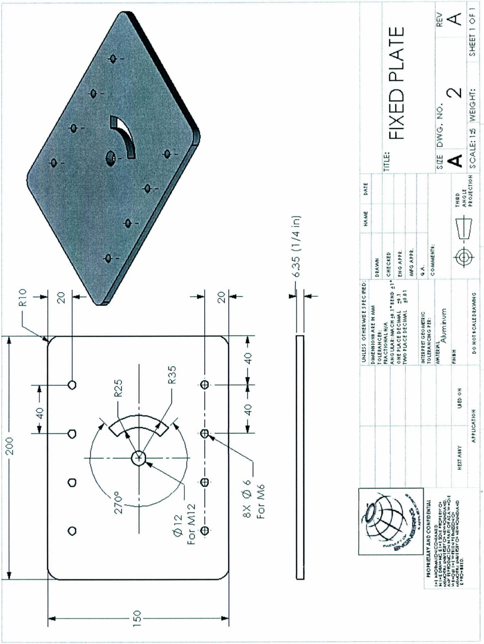

R10
20
20
200
40
40
40
R25
R35
270°
Ø12
For M12
8X Ø6
For M6
150
6.35 (1/4 in)
UNLESS OTHERWISE SPECIFIED:
DIMENSIONS ARE IN MM
TOLERANCES:
FRACTIONAL N/A
ANGULAR: MACH ±0.1° BEND ±1°
ONE PLACE DECIMAL ±0.1
TWO PLACE DECIMAL ±0.01
INTERPRET GEOMETRIC TOLERANCING PER:
MATERIAL
Aluminum
FINISH
NEXT ASSY
USED ON
APPLICATION
DO NOT SCALE DRAWING
NAME
DATE
DRAWN
CHECKED
ENG APPR.
MFG APPR.
Q.A.
COMMENTS:
THIRD ANGLE PROJECTION
TITLE:
FIXED PLATE
SIZE
A
DWG. NO.
2
REV
A
SCALE: 1:5
WEIGHT:
SHEET 1 OF 1
PROPRIETARY AND CONFIDENTIAL
1
2
3
4
5

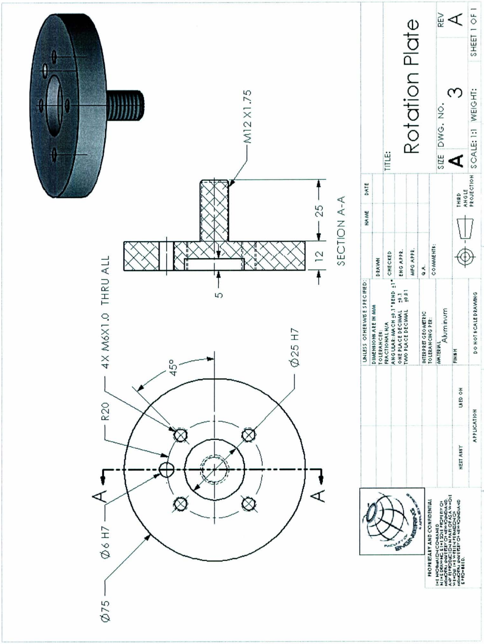
Ø75
Ø6 H7
A
A
R20
4X M6X1.0 THRU ALL
45°
Ø25 H7
M12 X1.75
5
12
25
SECTION A-A
UNLESS OTHERWISE SPECIFIED:
DIMENSIONS ARE IN MM
INTERPRET GEOMETRIC TOLERANCING PER:
MATERIAL
Aluminum
FINISH
DO NOT SCALE DRAWING
DRAWN
CHECKED
ENG APPR.
MFG APPR.
Q.A.
COMMENTS:
NAME
DATE
THIRD ANGLE PROJECTION
NEXT ASSY
USED ON
APPLICATION
PROPRIETARY AND CONFIDENTIAL
TITLE:
Rotation Plate
SIZE
A
DWG. NO.
3
REV
A
SCALE: 1:1
WEIGHT:
SHEET 1 OF 1

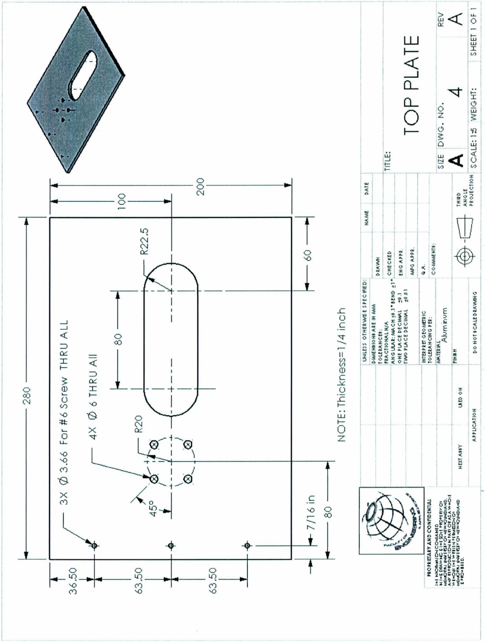
280
200
100
R22.5
60
80
3X Ø 3.66 For #6 Screw THRU ALL
4X Ø 6 THRU All
R20
45°
7/16 in
80
36.50
63.50
63.50
NOTE: Thickness=1/4 inch
UNLESS OTHERWISE SPECIFIED:
DIMENSIONS ARE IN MM
TOLERANCES:
FRACTIONAL N/A
ANGULAR: MACH ±0.1° BEND ±1°
ONE PLACE DECIMAL ±0.1
TWO PLACE DECIMAL ±0.01
INTERPRET GEOMETRIC TOLERANCING PER:
MATERIAL Aluminum
FINISH
DO NOT SCALE DRAWING
NEXT ASSY
USED ON
APPLICATION
DRAWN
CHECKED
ENG APPR.
MFG APPR.
Q.A.
COMMENTS:
NAME
DATE
THIRD ANGLE PROJECTION
TITLE:
TOP PLATE
SIZE A
DWG. NO. 4
REV A
SCALE: 1:5
WEIGHT:
SHEET 1 OF 1
PROPRIETARY AND CONFIDENTIAL
5
4
3
2
1

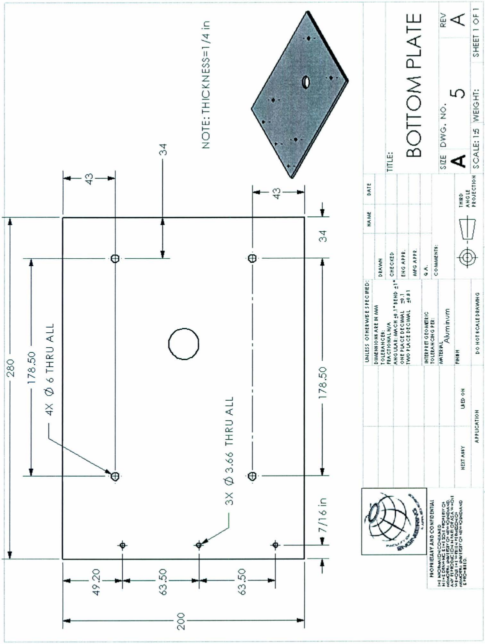
NOTE: THICKNESS=1/4 in
4X Ø 6 THRU ALL
3X Ø 3.66 THRU ALL
280
178.50
178.50
34
34
43
43
7/16 in
49.20
63.50
63.50
200
UNLESS OTHERWISE SPECIFIED:
DIMENSIONS ARE IN MM
TOLERANCES:
FRACTIONAL N/A
ANGULAR: MACH ±0.1° BEND ±1°
ONE PLACE DECIMAL ±0.1
TWO PLACE DECIMAL ±0.01
INTERPRET GEOMETRIC TOLERANCING PER:
MATERIAL
Aluminum
FINISH
DO NOT SCALE DRAWING
NAME
DATE
DRAWN
CHECKED
ENG APPR.
MFG APPR.
Q.A.
COMMENTS:
THIRD ANGLE PROJECTION
TITLE:
BOTTOM PLATE
SIZE
A
DWG. NO.
5
REV
A
SCALE: 1:5
WEIGHT:
SHEET 1 OF 1
NEXT ASSY
USED ON
APPLICATION
PROPRIETARY AND CONFIDENTIAL
1
2
3
4
5

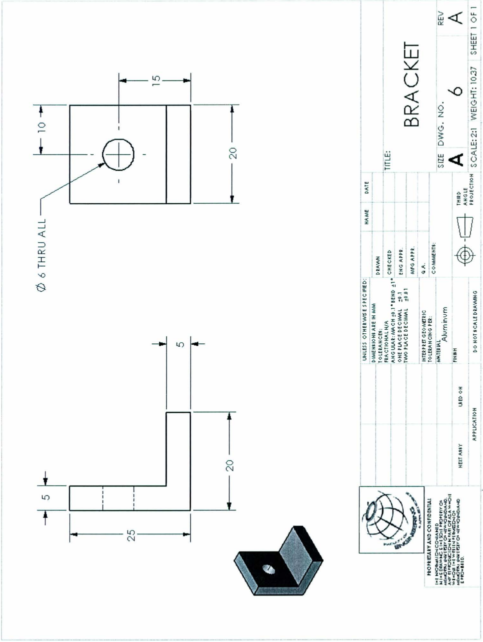

Ø 6 THRU ALL
10
15
20
5
5
20
25
UNLESS OTHERWISE SPECIFIED:
DIMENSIONS ARE IN MM
TOLERANCES:
FRACTIONAL N/A
ANGULAR: MACH ±0.1° BEND ±1°
ONE PLACE DECIMAL ±0.1
TWO PLACE DECIMAL ±0.01
INTERPRET GEOMETRIC TOLERANCING PER:
MATERIAL
Aluminum
FINISH
DO NOT SCALE DRAWING
DRAWN
CHECKED
ENG APPR.
MFG APPR.
Q.A.
COMMENTS:
NAME
DATE
THIRD ANGLE PROJECTION
TITLE:
BRACKET
SIZE
A
DWG. NO.
6
REV
A
SCALE: 2:1
WEIGHT: 10.37
SHEET 1 OF 1
NEXT ASSY
USED ON
APPLICATION
PROPRIETARY AND CONFIDENTIAL
FACULTY OF ENGINEERING
1
2
3
4
5

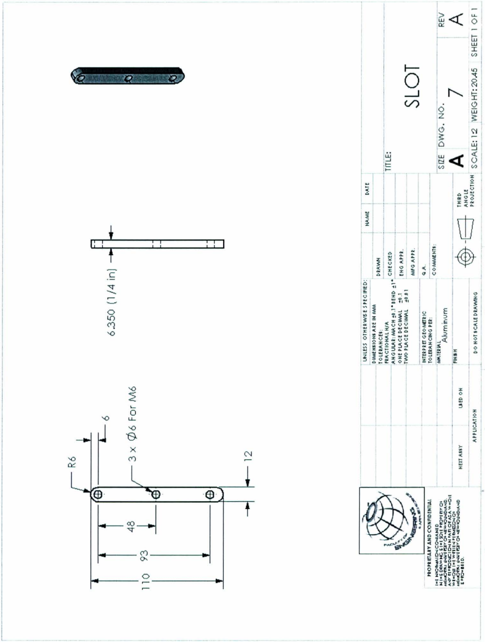
R6
6
3 x Ø6 For M6
12
48
93
110
6.350 (1/4 in)
UNLESS OTHERWISE SPECIFIED:
DIMENSIONS ARE IN MM
NAME
DATE
DRAWN
CHECKED
ENG APPR.
MFG APPR.
Q.A.
COMMENTS:
MATERIAL
Aluminum
FINISH
DO NOT SCALE DRAWING
NEXT ASSY
USED ON
APPLICATION
THIRD ANGLE PROJECTION
TITLE:
SLOT
SIZE
DWG. NO.
A
7
REV
A
SCALE: 1:2
WEIGHT: 20.45
SHEET 1 OF 1
PROPRIETARY AND CONFIDENTIAL

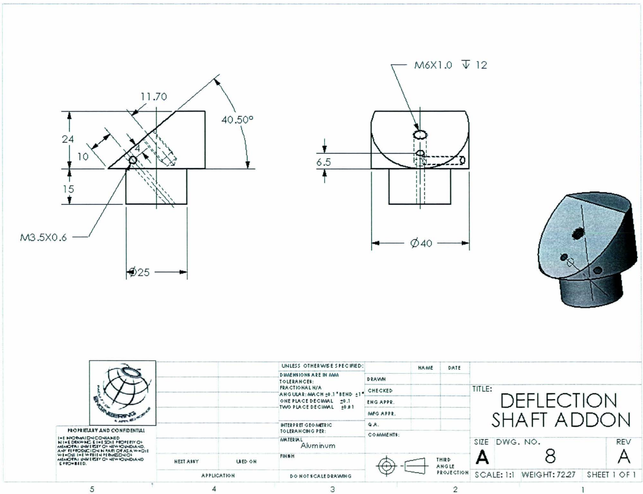
11.70
40.50°
24
10
4
15
M3.5X0.6
⌀25
M6X1.0 ↧ 12
6.5
⌀40
UNLESS OTHERWISE SPECIFIED:
DIMENSIONS ARE IN MM
TOLERANCES:
FRACTIONAL N/A
ANGULAR: MACH ±0.1° BEND ±1°
ONE PLACE DECIMAL ±0.1
TWO PLACE DECIMAL ±0.01
INTERPRET GEOMETRIC TOLERANCING PER:
MATERIAL Aluminum
FINISH
DO NOT SCALE DRAWING
NEXT ASSY
USED ON
APPLICATION
NAME
DATE
DRAWN
CHECKED
ENG APPR.
MFG APPR.
Q.A.
COMMENTS:
THIRD ANGLE PROJECTION
TITLE:
DEFLECTION SHAFT ADDON
SIZE A
DWG. NO. 8
REV A
SCALE: 1:1
WEIGHT: 72.27
SHEET 1 OF 1
PROPRIETARY AND CONFIDENTIAL
THE INFORMATION CONTAINED IN THIS DRAWING IS THE SOLE PROPERTY OF MEMORIAL UNIVERSITY OF NEWFOUNDLAND. ANY REPRODUCTION IN PART OR AS A WHOLE WITHOUT THE WRITTEN PERMISSION OF MEMORIAL UNIVERSITY OF NEWFOUNDLAND IS PROHIBITED.
5
4
3
2
1

A.2 Matlab Code in Slocum Glider modeling

```
function xdot=cylindricalmodeling(t,x);
xdot=zeros(12,1);
%%%%%%%%%Definition of the variables%%%%%%%%
% x(1)=x (X direction displacement) %
% x(2)=y (Y direction displacement) %
% x(3)=z (Zdirection displacement) %
% x(4)=phi (Roll angle) %
% x(5)=theta (Pitch angle) %
% x(6)=pha (Yaw angle) %
% x(7)=v1 (b1 velocity) %
% x(8)=v2 (b2 velocity) %
% x(9)=v3 (b3 velocity) %
% x(10)=omh1 (Roll angle rate) %
% x(11)=omh2 (Pitch angle rate) %
% x(12)=omh3 (Yaw angle rate) %
%%%%%%%%%Mass Term Definition%%%%%%%%
% mt -> Trimming mass %
% mL->Pitching battery mass %
% mc->Backward Battery mass %
% mpis->Pump pistion mass %
% mb -> Ballast tank mass %
%m-> water displacement mass %
%m0-> mass in the water %
%%%% %%% %%variable parameters% %%% %%% %%
m=52;                    %water displacement mass
```

```
rty=0;                          %trim mass lateral position
if t<424                        %Diving
    mb=0.233;                   %ballast tank mass
    rpLx=0.27732+0.0085;        %pitching battery position
else                            %Climbing
    mb=-0.233;
    rpLx=0.27732-0.0085;
end
%%%%%%%%Setting Battery Masses and Locations%%%%%%%%
mL=9.4;                         %pitching battery mass 9.4 kg
mc=7.6;                         %back battery mass 7.6kg
%%%Setting ballast tank location%%%
rbx=0.711;
rby=0;
rbz=0;
%%%Setting pitching battery pack location%%%
rpLy=0;
rpLz=0;
%%%Setting back battery pack location%%%
rpcx=-0.343;
rpcy=0;
rpcz=0.0095*m/mc;               %CG is low than CB with a vertical distance
%%%setup Trim weight and locations%%%
rtx=0;
rtz=0;
mt=1;
```

```
%%%Setting Hull Weight%%%
mh=34;
%%%%%%%%% Mass location vectors %%%%%%%%%
rb=[rbx;rby;rbz];                         %ballast tank
rpL=[rpLx;rpLy;rpLz];                     %pitch battery
rpc=[rpcx;rpcy;rpcz];                     %back battery
rt=[rtx;rty;rtz];                         %trim weight
rbover=[0 0 0;0 0 -rbx;0 rbx 0];
rpLover=[0 -rpLz 0;rpLz 0 -rpLx;0 rpLx 0];
rpcover=[0 -rpcz rpcy;rpcz 0 -rpcx;-rpcy rpcx 0];
rtover=[0 0 rty;0 0 0;-rty 0 0];
%%%%%%%%%Input slocum glider hydrodynamic parameters%%%%%%%%%
%%%masses and inertia%%%
m0=mb+mt+mh+mL+mc-m;                      %net weight
ms=mh;                                    %stationary mass=hull mass
%%%added mass%%%
mf1=5;
mf2=60;
mf3=70;
%%%added inertia%%%
J1=4;
J2=12;
J3=11;
%%%Hydrodynamic Coefficient in Table 2.3 on Page 28%%%
KL0=0;
KL=135+125;
```

```
KD0=2+1.4;
KD=45;
Kbeta=20;
KM0=0;
KM=-50;
KMY=100;
KMR=-60;
Kq1=0;
Kq2=0;
Kq3=0;
Komh11=-20;
Komh12=-60;
Komh13=-20;
Komh21=0;
Komh22=0;
Komh23=0;
g=9.8;
%%%Velocity vectors%%%
v=[x(7);x(8);x(9)];
vover=[0 -v(3) v(2);v(3) 0 -v(1);-v(2) v(1) 0];
omh=[x(10);x(11);x(12)];
omhover=[0 -omh(3) omh(2);omh(3) 0 -omh(1);-omh(2) omh(1) 0];
%%%%%%%%Kinematic Equation%%%%%%%%
R1=[cos(x(6))*cos(x(5)) -sin(x(6))*cos(x(4))+cos(x(6))*sin(x(5))*...
    ...sin(x(4)) sin(x(6))*sin(x(4))+cos(x(6))*sin(x(5))*cos(x(4))];
R2=[sin(x(6))*cos(x(5)) cos(x(6))*cos(x(4))+sin(x(6))*sin(x(5))*sin(x(4)) ...
```

```
    ...-cos(x(6))*sin(x(4))+sin(x(6))*sin(x(5))*cos(x(4))];
R3=[-sin(x(5)) cos(x(5))*sin(x(4)) cos(x(5))*cos(x(4))];
R=[R1;R2;R3];
Rs=[1 sin(x(4))*tan(x(5)) cos(x(4))*tan(x(5));0 cos(x(4)) -sin(x(4));...
    ...0 sin(x(4))/cos(x(5)) cos(x(4))/cos(x(5))];
Kinematic1=R*v;
Kinematic2=Rs*omh;
%%%%%%%%Hydrodynamic Matrix and Angles%%%%%%%%
tilt=transpose(R)*[0;0;1];
M=ms*diag([1,1,1])+diag([mf1,mf2,mf3]);
J=diag([J1,J2,J3]);
V=sqrt(x(7)^2+x(8)^2+x(9)^2);
alpha=atan(x(9)/x(7));
beta=asin(x(8)/V);
%%%%%%%%Stream coordinate transformation and forces%%%%%%%%
RWB=[cos(alpha)*cos(beta) -cos(alpha)*sin(beta) -sin(alpha);sin(beta) cos(alpha) 0;...
    ...sin(alpha)*cos(beta) -sin(alpha)*sin(beta) cos(alpha)];
D=(KD0+KD*alpha^2)*V^2;
SF=Kbeta*beta*V^2;
L=(KL0+KL*alpha)*V^2;
MDL1=Komh11*x(10)*V^2+KMR*beta*V^2;
MDL2=(KM0+KM*alpha+Komh12*x(11))*V^2;
MDL3=KMY*beta*V^2+Komh13*x(12)*V^2;
Fext=RWB*[-D;SF;-L];
Text=RWB*([MDL1;MDL2;MDL3]);
%%%%%%%%Dynamic Equation%%%%%%%%
```

```
Fover1=M*v+mL*(v+cross(omh,rpL))+mc*(v+cross(omh,rpc))+...
    ...mb*(v+cross(omh,rb))+mt*(v+cross(omh,rt));
Fover=cross(Fover1,omh)+m0*g*tilt+Fext;
Tover1=J*omh+mL*rpLover*(v+cross(omh,rpL))+mc*rpcover*(v+cross(omh,rpc))+...
    ...mb*rbover*(v+cross(omh,rb))+mt*rtover*(v+cross(omh,rt));
Tover2=-vover*M*v-mL*vover*omhover*rpL-mc*vover*omhover*rpc...
    ...-mb*vover*omhover*rb-mt*vover*omhover*rt;
Tover3=mL*g*rpLover+mc*g*rpcover+mb*g*rbover+mt*g*rtover;
Tover=cross(Tover1,omh)+Tover2+Tover3*tilt+Text;
DynamicMatrix11=M+mL*[1 0 0;0 1 0;0 0 1]+mc*[1 0 0;0 1 0;0 0 1]...
        ...+mb*[1 0 0;0 1 0;0 0 1]+mt*[1 0 0;0 1 0;0 0 1];
DynamicMatrix12=-mL*rpLover-mc*rpcover-mb*rbover-mt*rtover;
DynamicMatrix21=mL*rpLover+mc*rpcover+mb*rbover+mt*rtover;
DynamicMatrix22=J-mL*rpLover*rpLover-mc*rpcover*rpcover...
        ...-mb*rbover*rbover-mt*rtover*rtover;
DynamicMatrix=[DynamicMatrix11 DynamicMatrix12;...
        ...DynamicMatrix21 DynamicMatrix22];
Dynamic=inv(DynamicMatrix)*[Fover;Tover];
%%%%%%%%Equations sum up%%%%%%%%
xdot(1)=Kinematic1(1);
xdot(2)=Kinematic1(2);
xdot(3)=Kinematic1(3);
xdot(4)=Kinematic2(1);
xdot(5)=Kinematic2(2);
xdot(6)=Kinematic2(3);
xdot(7)=Dynamic(1);
```

```
xdot(8)=Dynamic(2);
xdot(9)=Dynamic(3);
xdot(10)=Dynamic(4);
xdot(11)=Dynamic(5);
xdot(12)=Dynamic(6);
```

A.3 Microcontroller Code

```
#include <avr/io.h>
#include <util/delay.h>
#include<avr/interrupt.h>
///////////////////Define Global Variables./////////////////////////////
char exciteD[]=0x00,(1«PD5),(1«PD3),(1«PD6);
char exciteB[]=(1«PB3),0x00,0x00,0x00;
int16_t current_step=0;
int track_step=0;
unsigned int speed_adjust_parameter;
///////////////////////////UART Initialization Function//////////////////
void uart_init()
    {
    UCSR0B=(1«TXEN0)|(1«RXEN0);             //tx enable and rx enable
    UCSR0C=(1«UCSZ00)|(1«UCSZ01);
    UBRR0L=0x81;                             //baudrate setting
    UBRR0H=0x00;
    DDRD|=0x02;                              //set PD3 as output
    }
```

```
///////////////////////UART Transimit Function////////////////////////////
void uart_tx(unsigned char data)
    {
    while(!(UCSR0A&(1«UDRE0)));                //Wait until Buffer is empty
    UDR0=data;                                //Set Buffer
    }
///////////////////UART Receive Function//////////////////////////////
unsigned char uart_rx(void)
    {
    while(!(UCSR0A&(1«RXC0)));                //Wait receive complete
    return UDR0;                               //Save the data
    }
///////////////Stepper Motor Initial Test///////////////////////
void motor_init()
    {
    unsigned char i;
    /////////Define the Output Pins/////
    DDRC|=(1«PC6);
    DDRB|=(1«PB3);
    DDRD|=(1«PD3)|(1«PD5)|(1«PD6);
    PORTD=0x00;
    PORTB=0x00;
    /////////Rotate Four Steps/////
    for(i=0;i<4;i++)
        {
        PORTD=0x00;
```

```
        PORTB=0x00;
        PORTC|=(1«PC6);
        PORTD|=exciteD[i%4];
        PORTB|=exciteB[i%4];
        _delay_ms(50);
        track_step=0;
        }
    }
////////////////////Stepper Motor Rotate Clockwise////////////////////////
void step_cw(unsigned char steps)
    {
    unsigned char i;
    /////////Define the Output Pins/////
    DDRC|=(1«PC6);
    DDRB|=(1«PB3);
    DDRD|=(1«PD3)|(1«PD5)|(1«PD6);
    PORTD=0x00;
    PORTB=0x00;
    //////////////////Send Rotation Signal///////////////////
    for(i=track_step;i<steps+track_step;i++)
        {
        PORTD=0x00;
        PORTB=0x00;
        PORTC|=(1«PC6);
        PORTD|=exciteD[i%4];
        PORTB|=exciteB[i%4];
```

```
        _delay_ms(40/speed_adjust_parameter);
        }
    track_step=i%4;
    }
////////////////////Stepper Motor Rotate Counter Clockwise////////////////////////
void step_ccw(unsigned char steps)
    {
    unsigned char i;
    /////////Define the Output Pins/////
    DDRC|=(1«PC6);
    DDRB|=(1«PB3);
    DDRD|=(1«PD3)|(1«PD5)|(1«PD6);
    PORTD=0x00;
    PORTB=0x00;
    //////////////////Send Rotation Signal////////////////////
    for(i=track_step;i<steps+track_step;i++)
        {
        PORTD=0x00;
        PORTB=0x00;
        PORTC|=(1«PC6);
        PORTD|=exciteD[3-i
        PORTB|=exciteB[3-i
        _delay_ms(40/speed_adjust_parameter);
        }
    track_step=3-i
    }
```

```
//////////////////////////Main//////////////////////////////
void main()
    {
    //////////////Define Motor Rotation Variables/////////////
    unsigned char direction;
    unsigned char step;
    unsigned int speed_adjust_parameter;
    uart_init();                    //Initialization
    motor_init();                    //Initialization
    _delay_ms(100);                    //short delay
    uart_tx(0xEE);                    //Acknowlegde byte to PC
    uart_tx(0x00);
    _delay_ms(100);
    uart_tx(0xEE);
    uart_tx(0xEE);
    _delay_ms(100);
    //////////////Define the Current Step Variable 16bits/////////////
    unsigned char current_step_L;
    unsigned char current_step_H;
    while(1)
        {
        //////obtain the commands from PC////////
        direction=uart_rx();
        _delay_ms(10);
        speed_adjust_parameter=uart_rx();
        _delay_ms(10);
```

```
step=uart_rx();
_delay_ms(10);
////////Switch the Direction////////////
//////01 Clockwise,
//////02 Counter Clockwise,
//////03 Clear the Current Steps data,
//////04 Motor Test, others Break////////
switch (direction)
    {
    case 0x01:
        step_cw(step);
        current_step=current_step+step;
        current_step_L=current_step&0xFF;
        current_step_H=(current_step»8)&0xFF;
        uart_tx(current_step_H);
        uart_tx(current_step_L);
        uart_tx(0xEE);
    break;
    case 0x02:
        step_ccw(step);
        current_step=current_step-step;
        current_step_L=current_step&0xFF;
        current_step_H=(current_step»8)&0xFF;
        uart_tx(current_step_H);
        uart_tx(current_step_L);
        uart_tx(0xEE);
```

```
            break;
                case 0x03://initial Parameter
                current_step_L=0x00;
                current_step_H=0x00;
                uart_tx(current_step_H);
                uart_tx(current_step_L);
                uart_tx(0xEE);
                break;
                case 0x04:
                motor_init();
            break;
            default;
            break;
            }
        }
    }
```